JGR Atmospheres

RESEARCH ARTICLE
10.1029/2019JD031791

Simulation of Atmospheric Microbursts Using a Numerical Mesoscale Model at High Spatiotemporal Resolution

Pedro Bolgiani[1], Sergio Fernández-González[2], Francisco Valero[1,5], Andrés Merino[3], Eduardo García-Ortega[3], José Luis Sánchez[3], and María Luisa Martín[4,5]

[1]Department of Earth Physics and Astrophysics, Faculty of Physics, Complutense University of Madrid, Madrid, Spain, [2]State Meteorological Agency (AEMET), Santander, Spain, [3]Atmospheric Physics Group, IMA, University of León, León, Spain, [4]Department of Applied Mathematics, Faculty of Computer Engineering, University of Valladolid, Valladolid, Spain, [5]Interdisciplinary Mathematics Institute, Complutense University of Madrid, Madrid, Spain

Key Points:
- The Weather Research and Forecasting numerical model is able to reproduce high-reflectivity microbursts
- The characteristic variables of the microburst are properly simulated, although some intensities are lower than observations
- Differences are observed between different microphysics and planetary boundary layer parametrizations

Correspondence to:
P. Bolgiani,
pbolgian@ucm.es

Citation:
Bolgiani, P., Fernández-González, S., Valero, F., Merino, A., García-Ortega, E., Sánchez, J. L., & Martín, M. L. (2020). Simulation of atmospheric microbursts using a numerical mesoscale model at high spatiotemporal resolution. *Journal of Geophysical Research: Atmospheres*, *125*, e2019JD031791. https://doi.org/10.1029/2019JD031791

Received 8 OCT 2019
Accepted 31 JAN 2020
Accepted article online 5 FEB 2020

Abstract Atmospheric microbursts are low-level meteorological events that can produce significant damage on the surface and pose a major risk to aircraft flying close to the ground. Studies and ad hoc numerical models have been developed to understand the origin and dynamics of the microburst; nevertheless, there are few researches of the phenomenon using global and mesoscale models. This is mainly due to the limitations in resolution, as microbursts normally span for less than 4 km and 20 min. In this paper, the Weather Research and Forecasting model is used at resolutions of 400 m and 3 min to test if it can properly capture the variables and dynamics of high-reflectivity microbursts. Several microphysics and planetary boundary layer parametrizations are tested to find the best model configuration for the simulation of this kind of episodes. General conditions are evaluated by using thermodynamic diagrams. Surface and vertical wind speed, reflectivity, precipitation, and other variables for each simulated event are compared with observations, and the model's sensitivity to the variables is assessed. The dynamics and evolution of the microburst is evaluated using different plots of a chosen event. The results show that the model is able to reproduce high-reflectivity microbursts in accordance with observations, although there is a tendency to underestimate the intensity of variables, most markedly on the wind vertical velocity. Regarding the microphysics schemes, the Morrison parametrization performs better than the WRF single-moment 6-class scheme. No major differences are found between the Mellor-Yamada-Janjic and the Mellor-Yamada-Nakanishi-Niino planetary boundary layer parametrizations.

1. State of the Art

Atmospheric *downbursts* are first noted in the scientific literature by Fujita (1976) and Fujita and Byers (1977), who describe it as an extremely intense *downdraft*, a negative vertical component of the wind vector (w), near the ground that can generate extensive damage on the surface and pose a risk to aircraft at low altitudes. The authors differentiate the phenomenon from the more common downdrafts generated by heavy precipitating convective cells, noted by Byers and Braham (1949). Then, Fujita and Byers (1977), Fujita (1981b), and Fujita and Wakimoto (1981) define a downburst as an atmospheric event where a strong downdraft in the lower heights of the atmosphere produces an area of damaging surface wind with a divergent pattern, ranging from less than one to tens of kilometers. These surface winds generate a toroidal shaped gust front (Fujita, 1981b; Fujita & Wakimoto, 1983), named outburst at first and *outflow* in the later literature. Fujita also creates a subdivision of downbursts based on the planetary horizontal scale of the outflow (Fujita, 1981b) and the duration of the peak winds (Fujita, 1980). Thus, a *macroburst* is defined by an outflow diameter larger than 4 km with peak winds lasting more than 5 min, while a *microburst* presents an outflow diameter smaller than 4 km and peak winds lasting less than 5 min. Downbursts can also be subdivided considering the amount of precipitation generated and the radar reflectivity of the convective cell (Fujita, 1985; Fujita & Wakimoto, 1981; Wilson et al., 1984). *Low reflectivity* or dry downbursts generate precipitation below 0.25 mm and radar reflectivity below 35 dBZ, while *high reflectivity* or wet downbursts present precipitation over 0.25 mm and radar reflectivity over 35 dBZ.

Microbursts are defined as a major meteorological hazard for aviation and flight safety (Fujita, 1980, 1981a, 1985; Wolfson et al., 1994). The phenomenon draws the attention of the aviation community and the

meteorological science in the decade of 1980, as it is related to several aircraft accidents and incidents. Thus, four major field programs are conducted to characterize the event, in which more than 300 microbursts are studied: the Northern Illinois Meteorological Research On Downbursts project (Fujita, 1985), the Joint Airport Weather Studies project (McCarthy et al., 1982; Wilson et al., 1984), the Federal Aviation Administration—Lincoln Laboratory Operational Weather Studies project (Wolfson et al., 1985), and the Microburst and Severe Thunderstorm (MIST) project (Atkins & Wakimoto, 1991; Dodge et al., 1986). These projects provide most of the information and technical knowledge of the microbursts, and their results have been verified by research in different countries as Japan (Ohno et al., 1996) and Australia (Potts, 1991). Along with the field programs, notable laboratory studies on the buoyancy and vertical acceleration of the air and ad hoc numerical models of the microbursts are developed by Srivastava (1985, 1987) and Proctor (1988, 1989).

Since the nineties the research in microbursts moves towards more practical approaches. McCann (1994) develops the Wind Index, and Pryor and Ellrod (2004) develop the Wet Microburst Severity Index, both forecasting algorithms to be used by operational meteorologists. Atlas et al. (2004) use Doppler radar observations to conclude the concurrence with Srivastava's models and that a narrow distribution of hail meteor sizes produces stronger high-reflectivity microbursts. Ferrero et al. (2014) perform laboratory simulations of microbursts to conclude that the fluid column height and density do not produce remarkable differences to the microburst, although high flow rotation can prevent the event, in contrast to former results. Pryor (2015) produces the Microburst Windspeed Potential Index as a nowcasting algorithm. Burlando et al. (2017) conduce a field study to confirm a high-reflectivity downburst event over Italy and the associated synoptic conditions.

With the development of high-performance computers, numerical models can reach high resolutions, and simulations are used in the research of the microburst. Lin et al. (2007) and Vermeire et al. (2011a) use subcloud idealized simulations to reproduce different microbursts' features generating results concurrent with observations. James and Markowski (2010) perform idealized three-dimensional simulations to find that, contrary to previous findings, dry air aloft is detrimental for downbursts as it reduces the hydrometeors' mass. Vermeire et al. (2011b) use large eddy simulations to model outflows with the conclusion that a cooling source model is better than and impinging jet model in capturing the features of the event. Nevertheless, Orf et al. (2012) perform a three-dimensional cloud simulation to prove that neither the impinging jet nor the cooling source models are sufficient to capture the complete process of downbursts, presenting results concurrent with observations. Oreskovic et al. (2018) also use cloud simulations to evaluate the thermodynamic cooling associated with downbursts. In the field of numerical weather prediction models, few publications are found on the microburst issue. A report by van Dijke et al. (2011) presents a high-resolution Weather Research and Forecasting (WRF) hindcast of a microburst event associated to a bow-echo structure, evaluating the winds and reflectivity of the event. A research by Carroll et al. (2011) shows a hit-or-miss test of four microphysics parametrizations, based on seven case studies, to conclude that the WRF single-moment 6-class scheme (WRF6) is the best performer. To the authors' knowledge, no research has been done to perform a detailed analysis of the variables and structure of the microburst using a mesoscale numerical model. Precisely, the objectives of this paper are to verify if the WRF model is able to reproduce high-reflectivity microbursts and evaluate the simulation of the main variables related. In addition, an assessment of two microphysics and two planetary boundary layer (PBL) parametrizations is performed. The paper is structured as follows: Section 2 presents a technical analysis of the microburst and the observational data used, both necessary to understand the assessment of the simulations, which are described in section 3 along with the evaluation process. Section 4 presents the results of the simulations and discussion of the evaluation, which lead to the conclusions in section 5.

2. The Microburst

Fujita (1985) and Wakimoto (1985) establish a series of conditions on the surface wind intensities to be considered a microburst, being the principal a minimum of 10 m s^{-1} at maximum wind speed (this would generate a radial difference in wind speed of $\Delta V \geq 20$ m s^{-1}). In addition, Wilson et al. (1984) and Hjelmfelt (1988) create the following characterization:

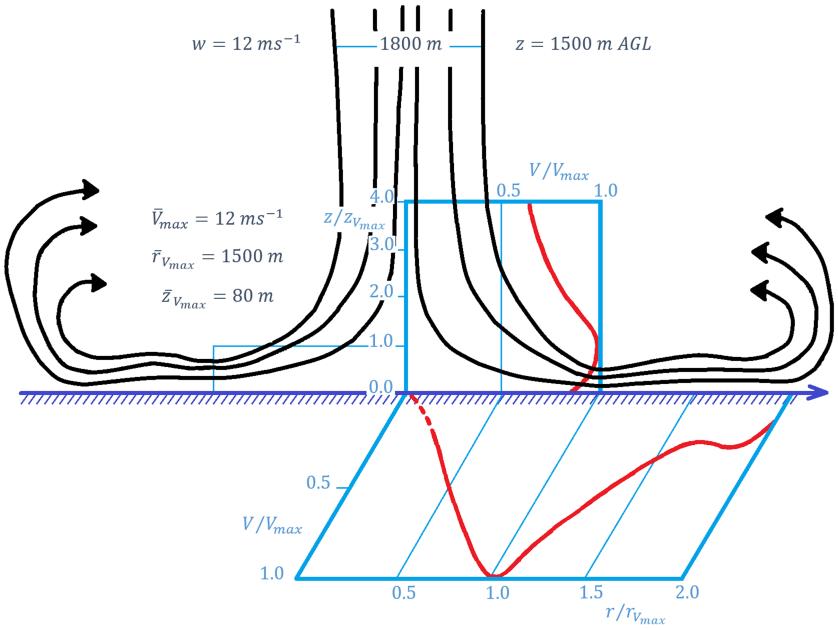

Figure 1. Vertical cross section of the characteristic microburst structure at maximum intensity. Based on a figure from Hjelmfelt (1988). © American Meteorological Society. Used with permission.

- Average maximum radial velocity differential: 24 m s^{-1}. Median: 22 m s^{-1}.
- Average distance of maximum radial velocity differential: 3,100 m.
- Average depth of outflow: 700 m.
- Characteristic lifespan:
- t = −5 min: downburst can be detected at 3.0 km above ground level (AGL) ($-5 \geq w \geq -10$ m s^{-1}).
- t = −2 min: downburst can be detected at 1.5 km AGL.
- t = 0 min: downburst reaches the surface; divergence appears in the surface wind field.
- t = +2.5 min: outflow reaches microburst wind speed ($\Delta V \geq 20$ m s^{-1}, $w \leq -10$ m s^{-1}).
- t = +7 min: outflow reaches maximum wind speed.
- t = +15 min: outflow decays under microburst intensity.

Figure 1 illustrates the characteristic downburst and outflow. Being the wind gust events most common during the summer (Kelly et al., 1985), a diurnal variation is also observed for the microburst, with 91% of occurrences between 10:00 and 21:00 local time (LT) and a peak observed between 14:00 and 16:00 LT (34% of events). Figure 2 presents the temporal frequency observed in the 297 microbursts registered in Northern Illinois Meteorological Research On Downbursts, Joint Airport Weather Studies (Fujita, 1985), and MIST (Atkins & Wakimoto, 1991).

Laboratory studies and numerical models of the microbursts developed by Srivastava (1985, 1987) and Proctor (1988, 1989) show that the microphysical and thermodynamic details are very important in the formation of a downdraft, which is governed by the inviscid vertical momentum equation (Wakimoto, 2001):

$$\frac{d\overline{w}}{dt} = -\frac{1}{\rho}\frac{\partial \overline{p}'}{\partial z} + g\left[\frac{\theta_v'}{\theta_{v0}} - \frac{c_v}{c_p}\frac{p'}{p_0} - (r_c + r_r + r_i)\right], \text{ Eq. (1)}$$

where w is vertical velocity, t is time, ρ is air density, p is pressure, z is height, g is gravity, Θ_v is the virtual potential temperature, c_p is specific heat at constant pressure, c_v is specific heat at constant volume, r_c is the mixing ratio of cloud water, r_r is the mixing ratio of rain water, and r_i is the mixing ratio of ice water. Primes denote differences with height. This makes four terms in the equation: perturbation pressure vertical gradient, thermal buoyancy, perturbation pressure buoyancy, and condensate loading. The vertical gradient of perturbation pressure is generally small and may be only considered in large mesoscale convective

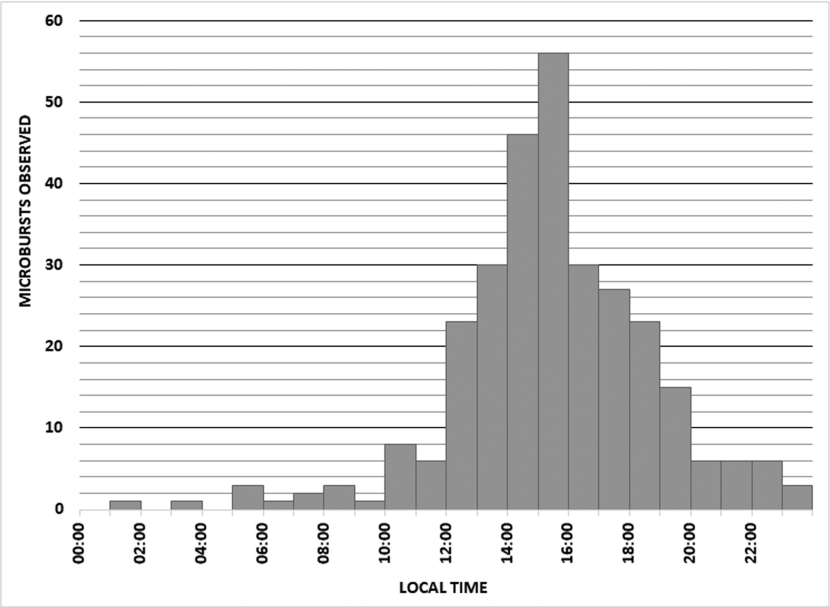

Figure 2. Temporal distribution of observed microbursts. Summation of data from NIMROD, JAWS, and MIST. JAWS = Joint Airport Weather Studies; MIST = Microburst and Severe Thunderstorm; NIMROD = Northern Illinois Meteorological Research On Downbursts.

systems and not for microbursts. The effects of pressure buoyancy are even smaller (Wakimoto, 2001) and should also be disregarded for the present study.

Downbursts usually initiate at midlevel layers, close above the 0 °C level (Proctor, 1989). Thermal buoyancy is the main factor in the downdraft due to the latent cooling generated by phase changes, although downdrafts tend to be notably subsaturated (Proctor, 1989; Srivastava, 1985) and not necessarily present a large negative buoyancy (Wakimoto, 2001). Compared with evaporation, melting and sublimation enhance downdraft speeds due to additional cooling (Proctor, 1988; Srivastava, 1987; Wakimoto et al., 1994); thus, snow conduces to strong low-reflectivity microbursts, and hail generates stronger high-reflectivity microbursts. Smaller drops have a large evaporative potential due to greater curvature, which leads to a larger equilibrium vapor pressure and lower relative humidity (Proctor, 1989; Srivastava, 1985, 1987). Also dependent on atmospheric meteors, condensate loading can initiate the downdraft or maintain it once initiated, in function of drop size, intensity, and downdraft speed (Byers & Braham, 1949; Knupp, 1988; Roberts & Wilson, 1989). Entrainment of environmental dry air at midlevel layers can initiate downdrafts by promoting evaporation. However, this effect may be detrimental at lower levels, where high relative humidity increases virtual ambient temperature, developing stronger downdrafts (Wakimoto, 2001).

Srivastava (1985) considers all these factors to produce a relationship between downburst speeds, temperature lapse rate, and liquid water mixing ratio (Figure 3), both measured at the 0 °C level. This relationship shows that thermal buoyancy (second term in equation 1) is dominant for low-reflectivity microbursts, but condensate loading (fourth term in equation 1) can override it in the initiation of high-reflectivity microbursts. The temperature lapse rate between 700 and 500 hPa is correlated with the occurrence of low-reflectivity microbursts, particularly when this lapse rate is observed to be smaller or equal to −8 °C km^{-1} in the afternoon (Caplan et al., 1990). In the case of high-reflectivity microbursts, the equivalent potential temperature (Θ_e) deficit, defined as the difference between the maximum Θ_e near the ground and the minimum Θ_e at midlevels, is more accurate. Afternoon environments conductive to high-reflectivity microbursts consistently exhibit Θ_e deficits equal or larger than 20 °C (Atkins & Wakimoto, 1991). The characteristic vertical thermodynamic diagrams for high-reflectivity microbursts are defined for temperature, dew point temperature, and Θ_e, as depicted in Figure 4.

Microburst models show that the downdraft accelerates in the lower levels of the atmosphere, reaching the maximum speed between 1,000 and 500 m AGL, thus the subcloud temperature lapse rate has to be less than

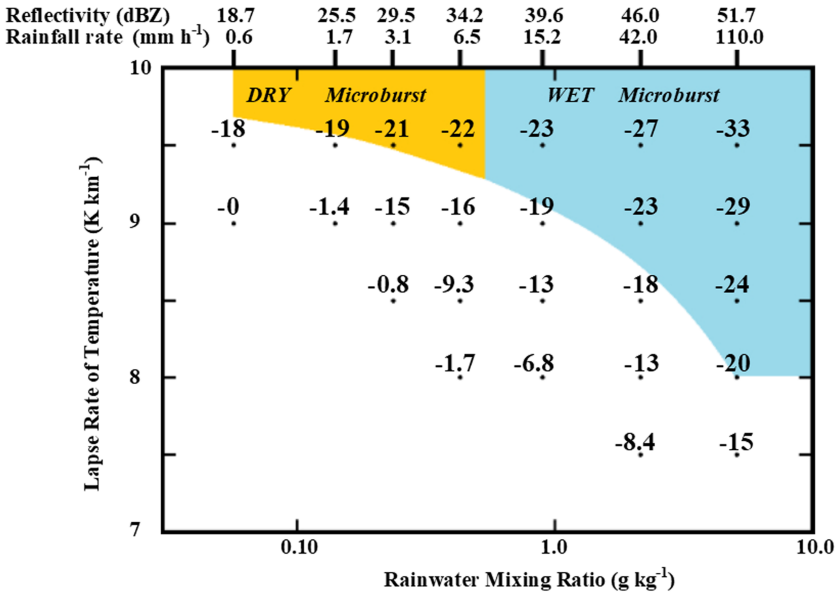

Figure 3. Results of a one-dimensional nonhydrostatic model of a downdraft. Plotted numbers show the vertical air velocity (m s^{-1}) at 3,700 m below the top of the downdraft as a function of environmental temperature lapse rate and liquid water mixing ratio at the top of the downdraft. Scales on top indicate radar reflectivity and precipitation rate at the top of the downdraft. Colored areas indicate microburst intensities as defined by Srivastava, colors differentiate between dry and high-reflectivity microbursts. Based on a figure from Srivastava (1985). © American Meteorological Society. Used with permission.

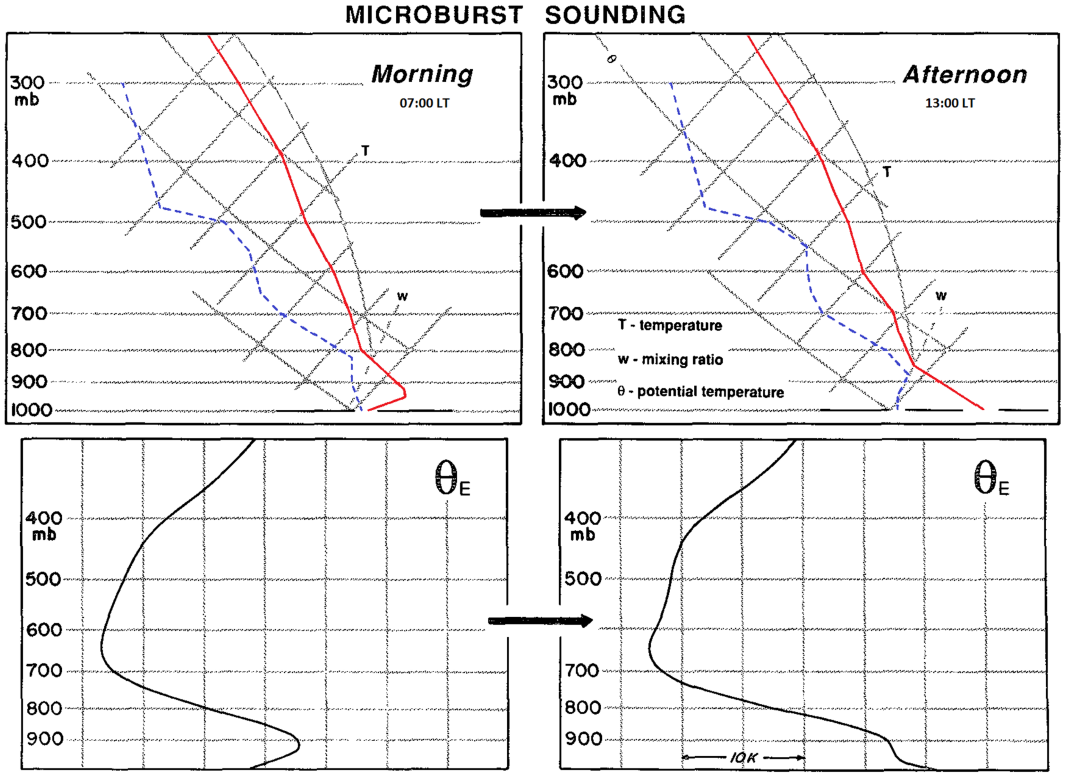

Figure 4. Characteristic thermodynamic diagrams for humid environments conductive to high-reflectivity microbursts. Upper plots depict temperature (red) and dew point temperature (blue). Lower plots depict equivalent potential temperature. Based on a figure from Atkins and Wakimoto (1991). © American Meteorological Society. Used with permission.

−7.5 °C km^{-1} for the evaporative cooling to support the downdraft (Proctor, 1988, 1989; Srivastava, 1985, 1987). It is also remarkable that, despite being one of the elemental components of microbursts, there is not a general agreement for the minimum w speed to the definition of the microburst. Fujita (1976) initially noted a minimum w for the downburst as −3.6 m s^{-1} at 90 m AGL. Hjelmfelt (1988) characterizes the microburst w speed as −12 m s^{-1} at 1,500 m AGL; later Wakimoto (2001) defines it as −20 m s^{-1}, but this is done in base of the arbitrary selection made by Srivastava (1985).

Finally, it has to be considered that microbursts typically develop in environments with weak wind shear (Johns & Doswell, 1992). The convective cells producing microbursts usually present vorticities comparable to the mesocyclones associated to tornadoes (Kessinger et al., 1988), although they show radial convergence aloft. In addition, some results support the concept of microbursts primarily occurring on new convective processes within existing outflow boundaries (Rydell & Ladd, 1991) or interacting with front leading edges (Wolfson, 1990).

2.1. Data: The MIST Project

The observational data used in this paper is gathered in one of the mayor projects performed in the study of microbursts. The MIST project (Atkins & Wakimoto, 1991; Dodge et al., 1986) is conducted in northern Alabama (United States of America) for 61 days during June and July 1986. The project uses an array of 41 surface stations operated by the National Center for Atmospheric Research (NCAR) and 30 stations operated by the Federal Aviation Administration—Lincoln Laboratory Operational Weather Studies. This mesoscalar network covers an area of approximately 40 × 30 km and is complemented with the data from three Doppler radar stations and the radiosonde data from the nearby Marshall Space Flight Center, operated by the National Aeronautics and Space Administration (commonly referred to as Redstone). A total of 62 microbursts were recorded in the project, 33 of them identified by the surface stations network, and 29 identified by the Doppler radar stations beyond the network's area (Atkins & Wakimoto, 1991).

The observations and results gathered during the MIST project become one of the original and main sources for high-reflectivity microburst characterization. Some of those observations are presented here to be used in the validation of the experiment. Particularly three dates have been selected as case studies (Atkins & Wakimoto, 1991), named with the number of microbursts observed:

- 13 July (MB25): This is the most active day in the project with 25 microbursts detected (40.3% of the total recorded by MIST). On this date the following data are observed, which will be used in the evaluation of the results of this paper:
  - Synoptic conditions are relatively stagnant, with a dry air inflow from the west into midlevels.
  - The cumulonimbus producing microbursts have tops reaching the tropopause.
  - Main precipitation cores are mainly composed of ice. They present reflectivities over 55 dBZ and extend between the level of minimum Θ_e and 7 to 10 km AGL.
  - During the descent of the precipitation core of the microbursts, environmental air is dragged into the core, at approximately the level of minimum Θ_e. This enhances negative buoyancy and accelerates the negative w.
  - Average maximum surface wind speed for microbursts: 15.1 m s^{-1}.
  - Average surface temperature difference for microbursts: −4.2 °C.
  - 13 microburst produce surface wind speeds over 15 m s^{-1}, five events reach over 20 m s^{-1}, only one microburst reaches over 25 m s^{-1}.
- 20 July (MB1): On this day a single microburst is observed, which is thoroughly documented and described (Kingsmill & Wakimoto, 1991; Wakimoto & Bringi, 1988).
- 10 June (MB0): This day is recorded as a thunderstorm day with no microbursts detection.

3. Experimental Design

The experiment consists in the numerical modelization of the three aforementioned days selected from the MIST project and the validation of these against the observational data. The simulations are performed with the Advanced Research WRF model version 3.7.1. This is a nonhydrostatic model that has been extensively proven and validated for weather prediction and research (Skamarock et al., 2008; Skamarock & Klemp, 2008). It is possible to fine-tune the model to local conditions using the multiple variables and

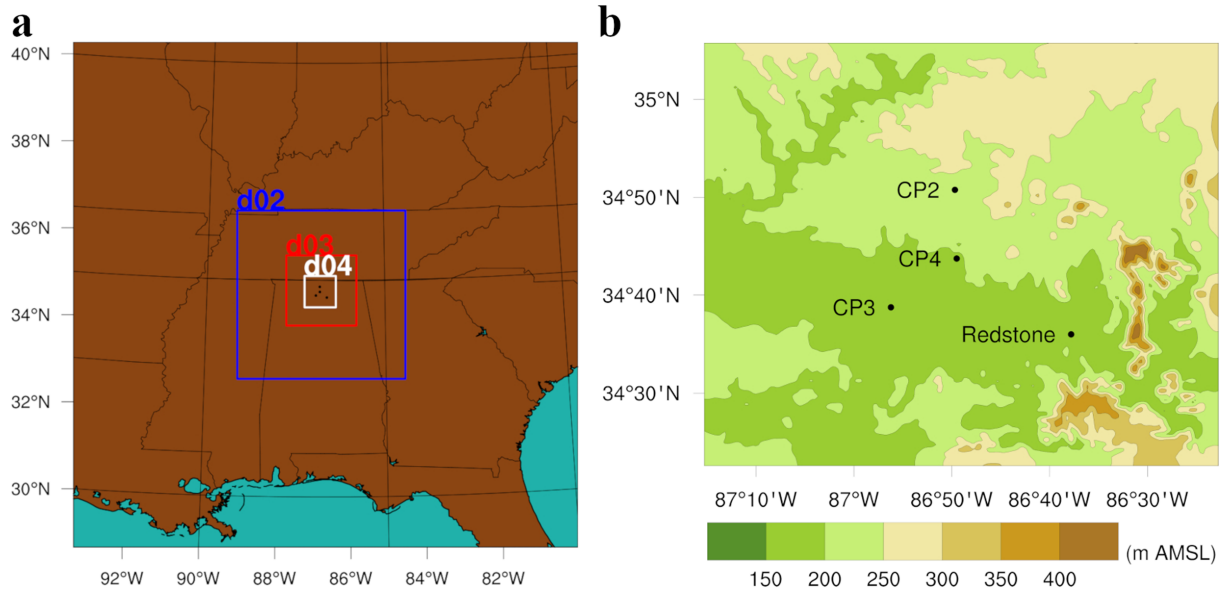

Figure 5. Area of study. (a) Positioning of the four nested domains used for the simulations (outer boundaries correspond to D1). (b) Terrain elevation map for D4. Black circles show the position of the MIST Doppler radar stations (CP2, CP3, and CP4) and the Redstone radiosonde site.

parametrizations available. In this study, two different PBL and two microphysics schemes are used, thus four simulations are presented for each date selected, making a total of 12 simulations.

3.1. Model Configuration and Parametrization

Initial and boundary conditions are taken from the Climate Forecast System Reanalysis developed by the National Center for Environmental Prediction. The reanalysis data is taken at 6-hr intervals with a surface spatial resolution of 0.312°, atmospheric spatial resolution of 0.5° and 37 vertical levels (Saha et al., 2010).

Four domains are allocated for the simulations, named D1, D2, D3, and D4 from outmost to innermost, with a two-way nesting strategy (Figure 5a). One of the challenges of this study is to work with spatial and temporal resolutions adapted to microburst events, so it can be determined if the WRF simulates it properly. The innermost domain (D4) is then configured as a 202 × 202 grid point domain with 400 m spatial grid resolution and 3 min of temporal resolution. D3 is 151 × 151 grid point with 1,200 m spatial resolution and 30 min temporal resolution. Outer domains are both 121 × 121 grid point with resolutions of 3,600 m, 60 min for D2 and 10,800 m, 180 min for D1. For vertical resolution, 60 sigma levels are defined from surface to 50 hPa, with a progressive resolution being greater in the lower levels of the troposphere, and four soil layers are used.

As high-reflectivity microbursts are related to heavy precipitation events (Fujita, 1985; Srivastava, 1985), parametrizations are chosen according to previous work by the authors to validate the model in similar conditions (Bolgiani et al., 2018). Long and short wave radiation scheme are new Goddard (Chou et al., 2001; Chou & Suarez, 1999) (called every 10 min), soil layers scheme (technically, land surface scheme) is unified Noah (Tewari et al., 2004), surface-atmosphere interface scheme (technically, surface layer scheme) is Eta similarity (Janjic, 1994), urban physics are not applied. Cumulus clouds are computed for D3 and D4, while the Grell-Freitas ensemble scheme (Grell & Freitas, 2014) is used for D1 and D2 (called every time step). The model is operated as nonhydrostatic in the four domains, with no *w* damping. For microphysics two schemes are used, being the moments computed the main difference between them. The Morrison scheme computes two moments (mixing ratio and number concentration of hydrometeors are independently predicted) and is proven to be a good performer in storm and trailing related precipitation (Morrison et al., 2009). The WRF6 scheme is a single-moment scheme (only mixing ratio is predicted) proven suitable for heavy precipitation forecasting (Hong & Lim, 2006). Both consider the same six different hydrometeors types: water vapor, cloud water, rainwater, cloud ice, snow, and graupel. For the PBL two schemes are used (called every time step),

both based on the Mellor-Yamada scheme. The Mellor-Yamada-Janjic (MYJ) scheme is proven suitable for forecasting the development and movement of severe storm (Janjic, 1994). The Mellor-Yamada-Nakanishi-Niino (MYNN) scheme is an improvement on buoyancy, stability, and turbulence kinetic energy formulations (Nakanishi & Niino, 2006). Thus, each date simulated is performed with the following configurations: Morrison-MYJ, WRF6-MYJ, Morrison-MYNN, and WRF6-MYNN. It has to be noted that initially other parametrizations were also tested, although they were discarded from the final experiment due to the poor performance shown in the preliminary results.

3.2. Area and Time of Study

The position of D4 corresponds to the geographical domain selected for this study, which is an 80 × 80-km square area, comprising the MIST Project surface network area and a buffer zone for radar detection beyond (Atkins & Wakimoto, 1991). This is centered near 086°50′W and 34°44′N, located west of the city of Huntsville, east of the city of Athens, and north of the Tennessee River (Figure 5b). The area is mostly a flat valley on a low plateau with elevations ranging from 150 to 300 m above mean sea level. Hills develop to the north and larger elevations to the east, reaching more than 400 m above mean sea level, where the outskirts of the Appalachian Mountains can be found. The climatology corresponds to a humid subtropical climate with hot and humid summers. For June and July the Huntsville International Airport (inside D4) reports the following daily averages: mean temperature 26.7 °C, maximum 32.4 °C, minimum 21.1 °C, wind speed 2.5 m s^{-1}, relative humidity 75%, and precipitation 1.9 mm (NWS, 2019). Thunderstorms are reported an average of 12.5 days per month.

The three case studies selected (see section 2.1) are simulated with a cold start from 01:00 to 01:00 LT the next day. This allows the model to spin up and reach the simulation daytime in stable conditions. It has to be noted that, regarding the diurnal variation of the microburst, local times are predominantly used in this paper, as they are more useful than Universal Time Coordinated (UTC). For the date and place of this study, LT = UTC–5 h.

3.3. Assessment Process and Methods

The evaluation of the simulations is done by steps, first evaluating the atmospheric general conditions, then the characteristic variables and finally the dynamics of the simulation. Data are processed and plotted using the NCAR Command Language software, version 6.6.2 (NCAR, 2019).

The environmental conditions are assessed by comparing the sounding data at 07:00 and 13:00 LT. Temperature, dew point, Θ_e, and Θ_e deficit are evaluated. In addition, the convective condensation level is determined as it is used as a reference height to evaluate microburst variables. After that, a count of microbursts generated by each simulation is performed using the surface wind field. It has to be noted that initially the surface wind divergence was evaluated to establish an objective threshold to define a microburst, but this was not possible due to the diversity of wind flows that can generate the same divergence values. Thus it was decided to perform this task by scanning the surface wind plot, searching for outflow patterns in each time step. Two conditions are required to be considered a microburst: First, a clear divergent wind pattern. Second, wind intensities equal or larger than 10 m s^{-1}, covering at least a 180° arc of the divergent flow ($\Delta V \geq 20$ m s^{-1}) (see example on Figure 9). Attending to the observations and times recorded for each date, the time window evaluated for this count ranges from 10:00 to 22:00 LT for MB0 and MB25, and from 11:00 to 18:00 LT for MB1. The results are evaluated against the number of microbursts observed each day. For comparison with further results, also the time steps which the microbursts span are taken into account; as the average lifetime of the microbursts is larger than the simulation's time step, a single event can be seen in several time steps of the simulation; also, several events can be found in the same time step.

To evaluate the characteristic variables of the microburst, an Eulerian approach is used, as this would be the kind of data recorded by a surface detection station. The grid location for the center of divergence of each simulated microburst is stablished, and over that point a data timeline is recorded for each characteristic variable: surface wind speed and direction (10 m AGL), minimum w between surface and 2,000 m AGL (based on results for the convective condensation level), maximum reflectivity between surface and 2,000 m AGL, temperature lapse rate between surface and 2,000 m AGL, precipitation, and surface temperature (2 m AGL). Every variable timeline is adjusted to the time step where maximum surface wind speed is achieved and a span of ±30 min is taken. Timelines are plotted, averages and standard deviations are

computed for every simulation. These data are used to evaluate the performance of each model parametrization.

In addition, probable wind gusts are calculated to assist in the wind speed evaluation. This is done by using a Weibull cumulative distribution function.

$$CDF(X) = 1 - e^{-\left(\frac{X - X_0}{\beta}\right)^{\alpha}} \quad \text{Eq. (2)}$$

The parameters used for the equation are proved in the estimation of wind gusts by the Air Force Weather Agency (Creighton et al., 2014), being $\alpha = 3.0$, $\beta = X_0^{0.75}$, and X_0 the maximum sustained surface wind speed during the time step considered (a variable computed by the model). The required probability is 0.95.

After this, the sensitivity of the model to the variables is evaluated with an automatic detection script. The script is designed to perform a test on the variables selected and yield a warning on each time step the conditions established are met in any grid point of the domain. In case several variables are requested, the script only yields a warning if every condition is met over some grid point. If every condition is met on the domain but on scattered grid points and no single grid point reunites all the variables, there is no warning. Based on results of the previous evaluation of *w*, three threshold speed are selected to test minimum *w* individually: −3, −6, and −9 m s^{-1}. Every other variable is individually tested at the defined characteristic or mean value. Then, variables are combined, using *w*, reflectivity, and temperature lapse rate to test the downburst and wind speed, surface temperature anomaly, and precipitation to test the outflow.

Finally, a single simulated microburst is used to evaluate the performance of the model on the structure and dynamic of the event against an observed microburst. The observation of MB1 is chosen for this assessment precisely because only one microburst was recorded, and it is properly documented (Kingsmill & Wakimoto, 1991; Wakimoto & Bringi, 1988). Thus, if we did not account for natural variability and other factors, a "perfect" simulation would reproduce a single microburst with similar characteristics. The simulation to evaluate is selected from the best performing parametrizations. The life cycle of the high-reflectivity microburst is systematically plotted with horizontal and cross-section figures showing the evolution of several variables. In this case, a Lagrangian approach is taken following the divergent center as it moves. Three different plots are produced for each time step. A north-south vertical cross section over the divergence center is used to depict the wind flow, *w* speeds, reflectivity, water, and ice content. A horizontal plot shows the surface wind vectors and speed. Another horizontal plot depicts the wind vectors and contours the fields, where the characteristic variables are met.

4. Results and Discussion

It has to be noted that the results presented in this section do not follow the same order in which they were achieved as described in section 3.3. First, the thermodynamic diagrams are shown, followed by the dynamic evaluation, and then by the characteristic variables and the variables sensitivity. Following this order allows a better understanding of the variables evaluation, as the reader will have a previous example to visualize.

4.1. Thermodynamic Diagrams

Figure 6 shows the simulated skew-T log-P diagrams at 07:00 and 13:00 LT for the four parametrizations on every date. The soundings are simulated over Redstone, as it is performed during the MIST Project. The results for each day are very similar for every simulation at 07:00 LT. The differences that can be noted at 13:00 LT are mainly due to the microphysics parametrization, as the PBL parametrizations only create remarkable differences for the dew point temperature above 700 hPa. In addition, every simulation creates a midlevel temperature inversion, also present at 07:00 LT for MB1 and MB0, not recorded in the observed thermodynamic diagrams for any date (Atkins & Wakimoto, 1991); they also produce a lower relative humidity than recorded near the 0 °C level. This makes the diagrams to perform worse above 700 hPa. It is noteworthy that this inversion is reducing the convective available potential energy, which should hinder

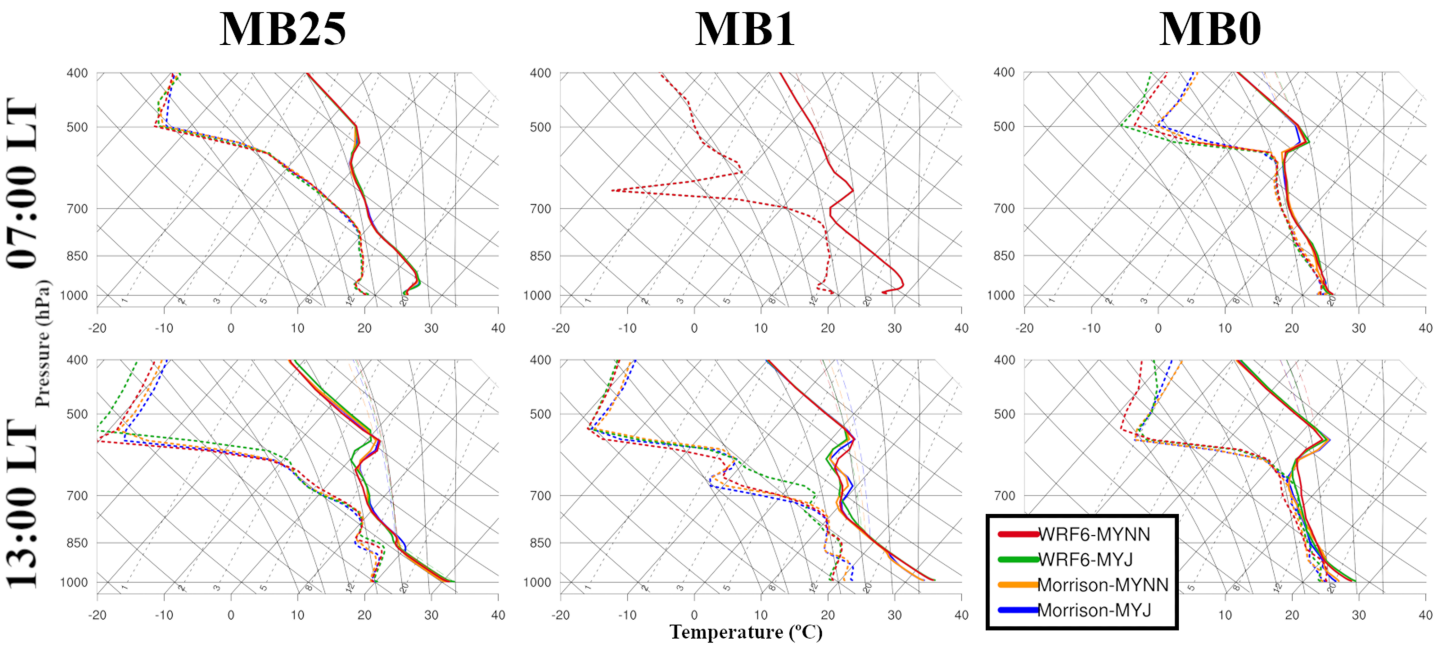

Figure 6. Thermodynamic diagrams for each date at morning and afternoon. Each diagram comprises temperature (solid lines), dew point temperature (short dashed lines), and CAPE (long dashed thin lines) for every parametrization used as per legend.

the generation of microbursts, while at the same time the dry layer is fostering the evaporation, which should enhance latent cooling.

Considering only the lower troposphere, the results for MB25 and MB1 show profiles similar to the characteristic inverted V described as conductive to high-reflectivity microbursts (Figure 4), properly reproducing the low-level temperature inversion in the morning diagram and the subcloud dry-adiabatic layer in the afternoon. The morning inversions are due to radiation and disappear as surface heating promotes convection. The large differences between the morning and afternoon diagrams for MB1 seem to respond to a deep convective situation, that forces the dry midlevel capping to higher levels. The simulations for MB0 also reproduce correctly the thermodynamic diagram in the lower troposphere with very small differences among them; particularly, the Morrison microphysics produces for 07:00 LT a small inversion below 970 hPa similar to the data presented by Atkins and Wakimoto (1991), although at 13:00 LT WRF6 is closer to observations in temperature values near the ground, producing a more accurate temperature lapse rate. The convective condensation level is computed for every date at 13:00 LT, being the highest result approximately 800 hPa. This correlates with a height of 2,000 m, which is used to evaluate *w*, reflectivity, and temperature lapse rate. It has also to be noted that the dry level at 13:00 LT is between 600 and 500 hPa.

Figure 7 shows the Θ_e diagram for the four different simulations at 07:00 and 13:00 LT on every date. The Θ_e diagrams present patterns similar to those described by Atkins and Wakimoto (1991), particularly for MB25 and MB1. It is remarkable that the different parametrizations produce very similar diagrams at 07:00 LT, in fact for MB1 they are exactly the same. Every diagram at 07:00 LT shows the low-level inversion described in the characterization (Figure 4), although most of them produce an unstable layer below 900 hPa not recorded in the observations. On MB0 and MB1 profiles present anomalies in midlevels, rendering the Θ_e deficit value unreliable. The results for 13:00 LT yield a poor performance on low levels. The stability of the layer is not properly reproduced for any day, although the general profile is similar to those recorded by Atkins and Wakimoto (1991). Evaluating the Θ_e deficit at 13:00 LT the WRF6 microphysics yields very similar values for every study case, above the 20 °C characteristic threshold. The Morrison parametrization generates different values for each case, only reaching the defined threshold on MB25 and MB1, in line with what this value is expected to do on microburst conducing situations. Nevertheless, it tends to overestimate the values on MB0 and MB1 for both PBL schemes, according to the profiles observed (Atkins & Wakimoto, 1991).

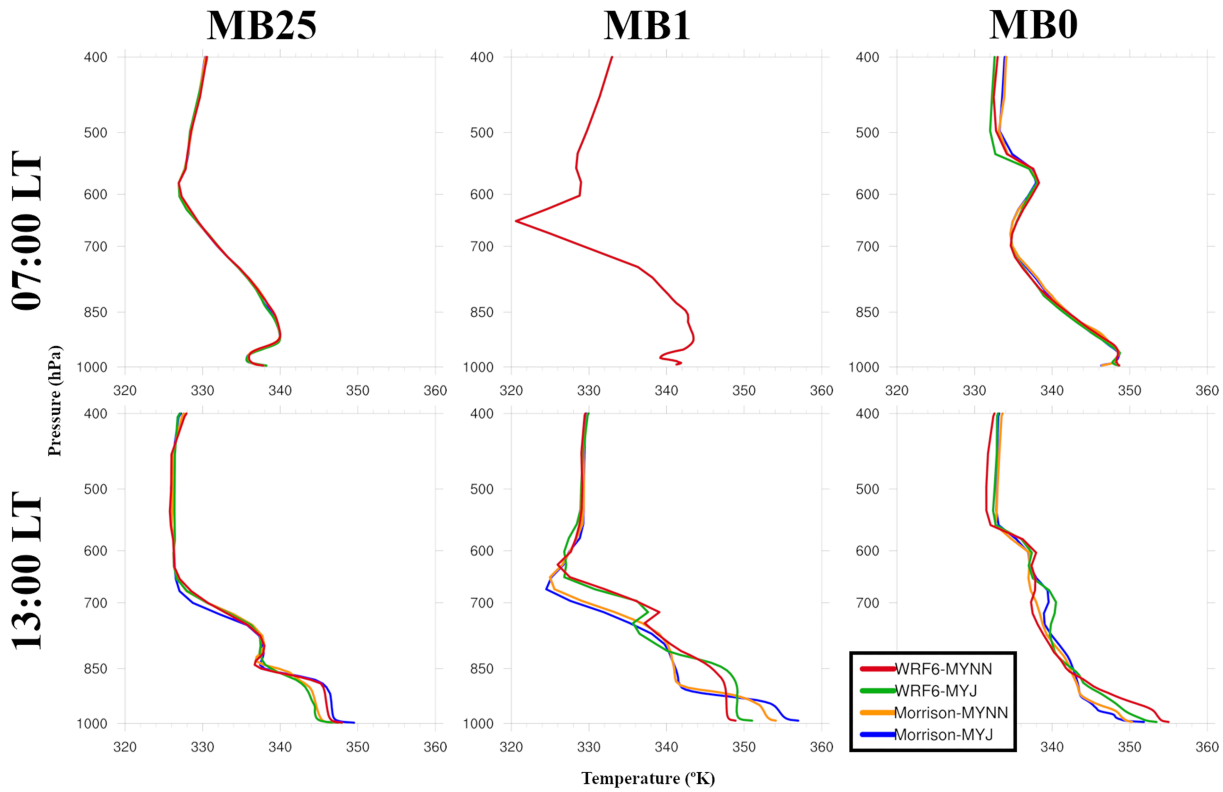

Figure 7. Equivalent potential temperature diagrams for each date at morning and afternoon. Each diagram comprises every parametrization used as per legend.

4.2. Morrison-MYJ Simulation for MB1

The reasons to select the Morrison-MYJ simulation for the dynamics assessment are deducted from results presented in the following subsections. In brief, no definitive conclusions can be taken from the variables assessment, as no one presents a clear difference between parametrizations to select one as best performer. Nevertheless, the Morrison microphysics generally outperforms the WRF6. Then, to choose the best model configuration, we have to use the initial count based on divergence (section 4.3). From these results it is evident that the Morrison-MYJ has to be selected, as the Morrison-MYNN produces no microbursts on MB1.

On MB1, the MIST project records a single high-reflectivity microburst from 14:19 to 14:28 LT, which is extensively documented by radar and direct observation (Kingsmill & Wakimoto, 1991; Wakimoto & Bringi, 1988). The event takes place to the north east of the geographical domain, outside the mesoscalar surface network, but it is detected by the three Doppler radar stations. The Morrison-MYJ simulation produced three different microbursts on MB1, at 12:42, 13:00, and 13:24 LT, all of them in the north east corner of D4. From these, the one simulated at 13:03 LT is chosen, as it is the best defined. Figures 8 and 9 present the life cycle of the simulated high-reflectivity microburst.

The cross sections at 12:51 and 12:54 LT (not shown) display a 50 dBZ core descending from 550 to 700 hPa as it travels south. At 12:57 LT (Figure 8) the nucleus of the convective cell is formed by ice above 600 hPa and water below, which is already initiating precipitation. A strong updraft is present in the upper part of the core, air entrainment is taking place from the north at 700 hPa and the influence of the outflow produced by another microburst can be seen to the north at low levels. At 13:00 LT the precipitation shaft reaches the surface, and the downdraft is properly formed with w below -6 m s^{-1}, pulling down the reflectivity core. The initiation of surface divergence can be seen at low levels, as well as an updraft to the north of the microburst due to the interaction with a former outflow. At 13:03 LT the downdraft attains maximum intensity, with w under -9 m s^{-1} very close to the ground. The cross section shows an approximately 2-km wide precipitation shaft, the 50 dBZ core reaching the ground, divergent winds near the surface, a 4- to 5-km wide outflow and weak updrafts generated by it at both sides. At 13:06 LT the ice over 600 hPa has depleted,

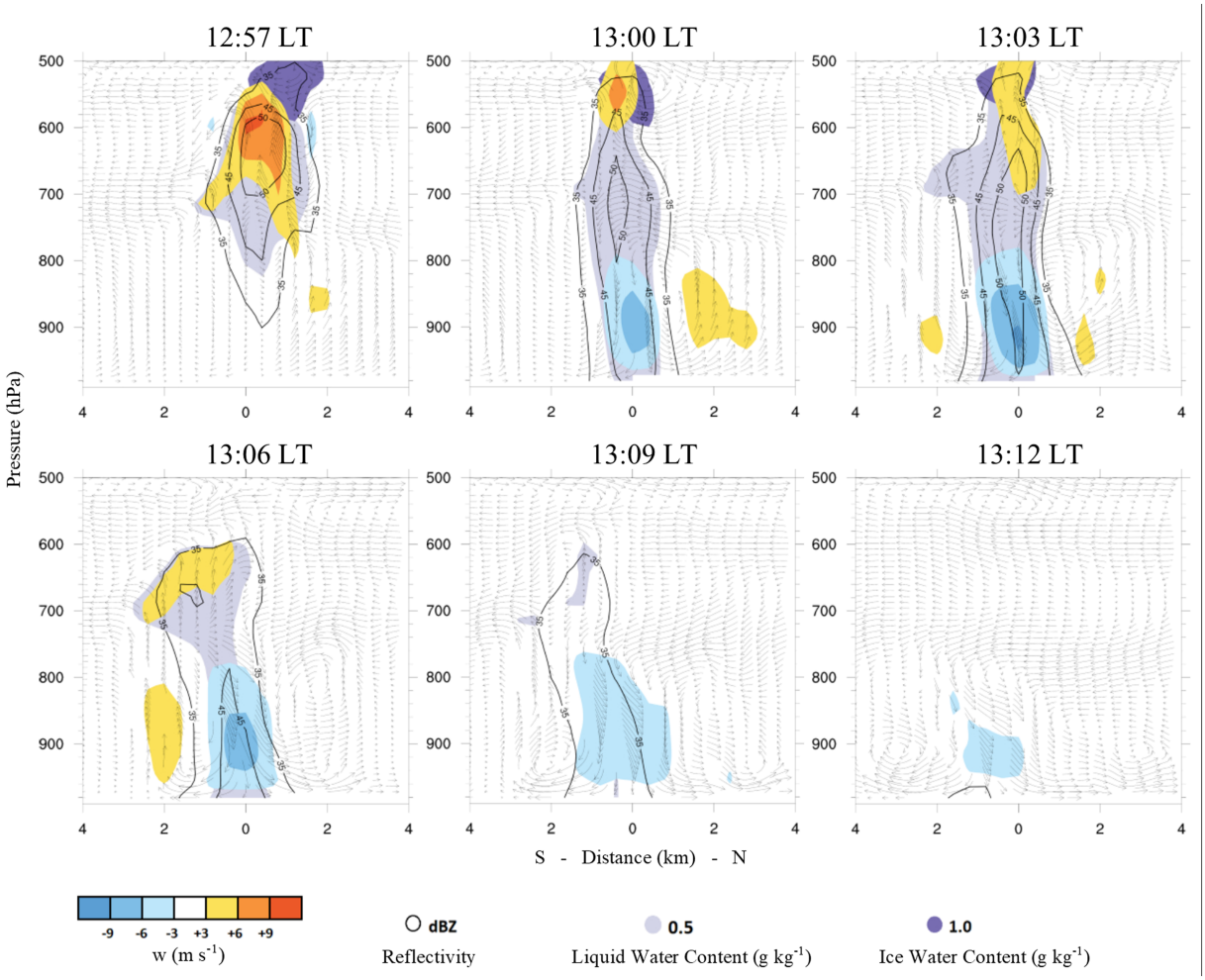

Figure 8. Vertical cross section for a Morrison-MYJ simulated microburst event, at 3-min intervals, depicting wind vectors, *w*, reflectivity, liquid, and ice water content, as per legend. Surface scale is km from the center of divergence. Plots correspond to sections depicted in Figure 9.

the reflectivity core is collapsing, and the *w* is receding back to 6 m s^{-1}. The outflow is approximately 5-km wide and 800-m deep. At 13:09 LT the downdraft is quickly dissipating and the liquid water content is almost zero, with no reflectivity over 45 dBZ. Divergence and outflow are still visible. At 13:12 LT only a few perturbations below 900 hPa remain, although divergence is present in the surface wind.

The plots in Figure 9 depict the surface wind vectors for the Morrison-MYJ simulation on MB1, the wind speed and several contours, properly reproducing the event. At 12:57 LT the temperature lapse rate near the microburst is still below −7.5 °C km^{-1} (no green contours can be seen near the black line). The 35 dBZ core has descended below 2,000 m AGL (orange contour). The outflow produced by another microburst can be seen to the north east. Despite the low-level winds depicted in the cross section (Figure 8), at 13:00 LT divergence cannot be properly seen in the surface wind field. Nevertheless, at this time, precipitation has reached the ground (light blue contour) and a shaft of minimum *w* below −6 m s^{-1} can be seen (dark blue contour). At 13:03 LT the surface wind field properly generates the divergence and the wind speeds of the microburst outflow, with the center of divergence reaching over 15 m s^{-1}. First pools of cold air appear near the microburst center (yellow contour), and this cooling makes the temperature lapse rate to reach above −7.5 °C in some spots (green contour). In addition, the precipitation, reflectivity, and *w* contours widen, which shows an intensification of these variables correlated with the cross section (Figure 8). At 13:06 LT the outflow reaches maximum intensity with wind speeds over 15 m s^{-1} near the microburst divergent center (Figure 9). The pools of cold air near the surface are evident, and the *w* weakens. At 13:09 LT divergence

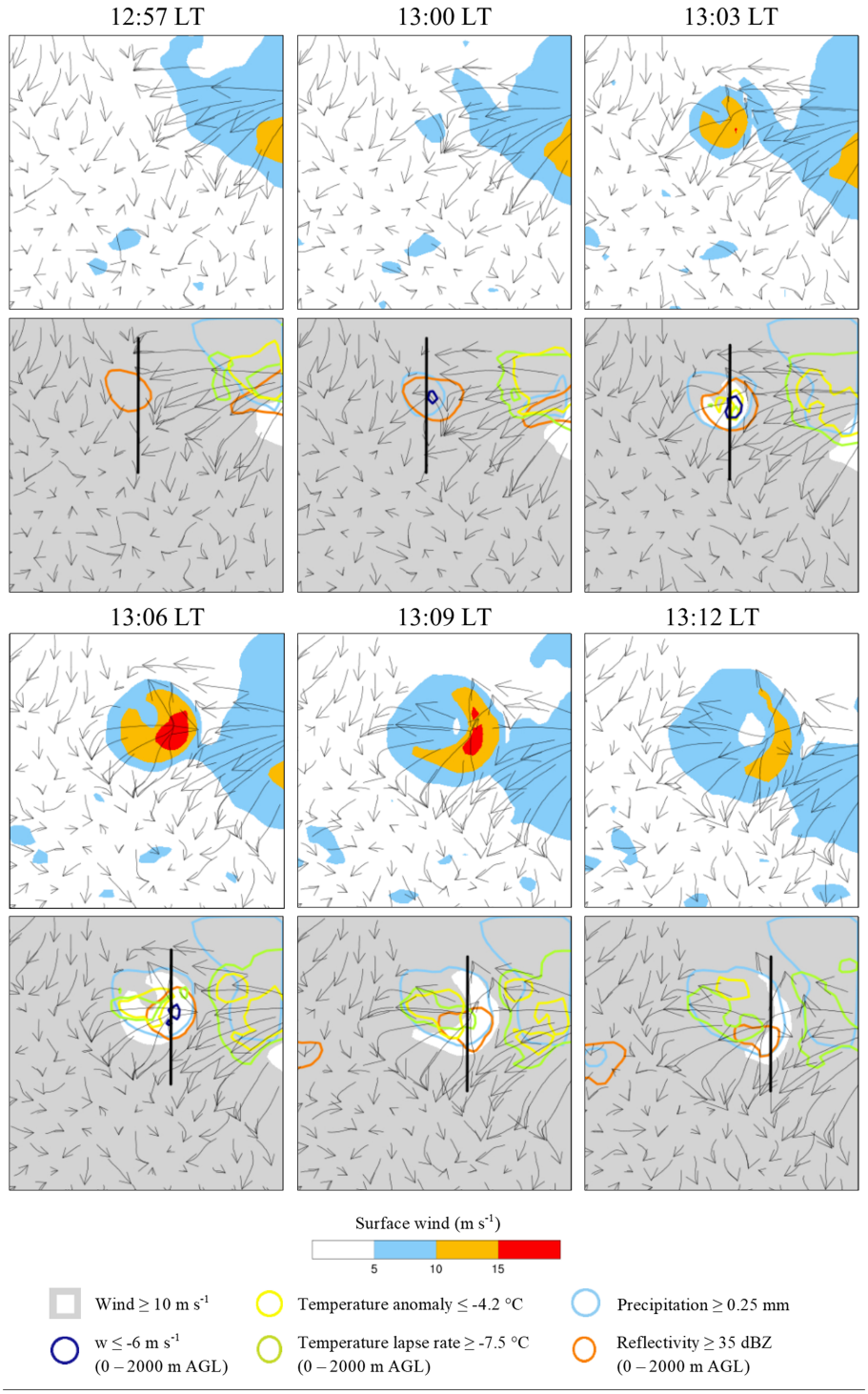

Figure 9. Horizontal plots depicting the surface wind vectors for a Morrison-MYJ simulated microburst event, at 3-min intervals. Top: wind speeds, as per legend. Bottom: contours of areas where each variable meets the defined thresholds, as per legend. The black line depicts the section used for vertical cross section in Figure 8.

and outflow are still visible, but the wind speed intensity is already decreasing, and the minimum w shaft is above -6 m s^{-1}, in correlation with the cross section (Figure 8). At 13:12 LT the divergence is present in the surface wind, but it cannot be considered a microburst anymore as most of the outflow is below 10 m s^{-1} in wind speed.

Table 1
Number of Microbursts Simulated for Each Date by Every Parametrization Used. Note. Time steps comprised by those microbursts and local time window in which they are generated. The name for each study case indicates the number of microbursts observed for that date.

Simulation parameters	Study cases								
	MB25			MB1			MB0		
	Microbursts	Time steps	Local time	Microbursts	Time steps	Local time	Microbursts	Time steps	Local time
Morrison-MYJ	22	35	15:00–19:00	3	9	12:00–14:00	0	/	/
Morrison-MYNN	14	32	15:00–19:00	0	/	/	1	3	20:00–21:00
WRF6-MYJ	75	108	12:00–19:00	97	84	11:00–18:00	12	25	13:00–20:00
WRF6-MYNN	44	68	12:00–18:00	53	72	12:00–17:00	14	54	10:00–19:00

Overall, the WRF model can properly simulate the dynamics of the high-reflectivity microburst. The timing and dimensions correspond to the microburst characterization, the water phases and reflectivity core evolution is according to the described process, midlevel air entrainment can be seen, the acceleration of the downdraft below the cloud base is evident (Figure 8), a well-defined outflow is simulated, reaching $\Delta V \geq 30$ m s^{-1} across the divergent center (Figure 9). It can even be argued if the microburst generates from the flow interaction with the previous outflow boundary.

Comparing with the observations (Kingsmill & Wakimoto, 1991; Wakimoto & Bringi, 1988), the simulation takes place 80 min before the recorded microburst and in the same quadrant of the domain field, although farther from the surface network than registered. It is remarkable that the microburst detected is generated by a convective cell growing next to an older cell, situated north east from it. Despite this older cell does not produce any microburst as the model does, the simulation properly generates both convective systems. The simulation displays a general wind flow similar to the conditions described by Wakimoto and Bringi (1988), and the 0 °C level is close to the observed level at 550 hPa. Although Kingsmill and Wakimoto (1991) show the reflectivity core reaching higher than 10 km AGL, the reflectivity values, timing and heights of the base of the core descending to the ground are very close to the radar data gathered. The *w* values derived from the radar also show large positive intensities above 5 km AGL before the microburst and negative values only below 2.5 km AGL at microburst intensity, as the model depicts.

4.3. Characteristic Variables

Table 1 summarizes the results of the surface wind divergence and speed evaluation. The Morrison-MYJ simulation yields 22 microbursts for MB25, 3 for MB1, and 0 for MB0 (35, 9, and 0 time steps, respectively), very close to the numbers of events observed (Atkins & Wakimoto, 1991). The Morrison-MYNN simulation presents an underestimation for MB25 and MB1, while it simulates a single microburst for MB0. Both WRF6 simulations produce a large overestimation, most notable on MB1 where WRF6-MYJ generates 97 microbursts and WRF6-MYNN simulates 53 events.

These results show a clear difference between microphysics parametrizations, with a marked overestimation for WRF6, which immediately renders this microphysics parametrization as a poor performer for this study. The PBL parametrizations yield more similar results but a tendency of underestimation for MYNN. Morrison-MYNN yields tolerable results overall, and the underestimation presented on MB25 and MB1 would be acceptable but for the fact that it generates one microburst on MB0, where the mesoscale conditions simulated are not conductive to microburst at all. Morrison-MYJ is the best performer, presenting the results most similar to observations. It is remarkable that the simulations generate the microbursts in local time windows very close to those recorded by Atkins and Wakimoto (1991) and in line with Figure 2.

Before evaluating the variables depicted in the following figures, a consideration of the method used for the assessment has to be made. As the selected grid point is approximately the center of the microburst and this may not be the most critical point for every variable, some values may not be properly represented. Even more, some microbursts travel notably during their life span due to the prevailing winds, which alters the results shown over time. Thus, the values produced may not show the complete picture

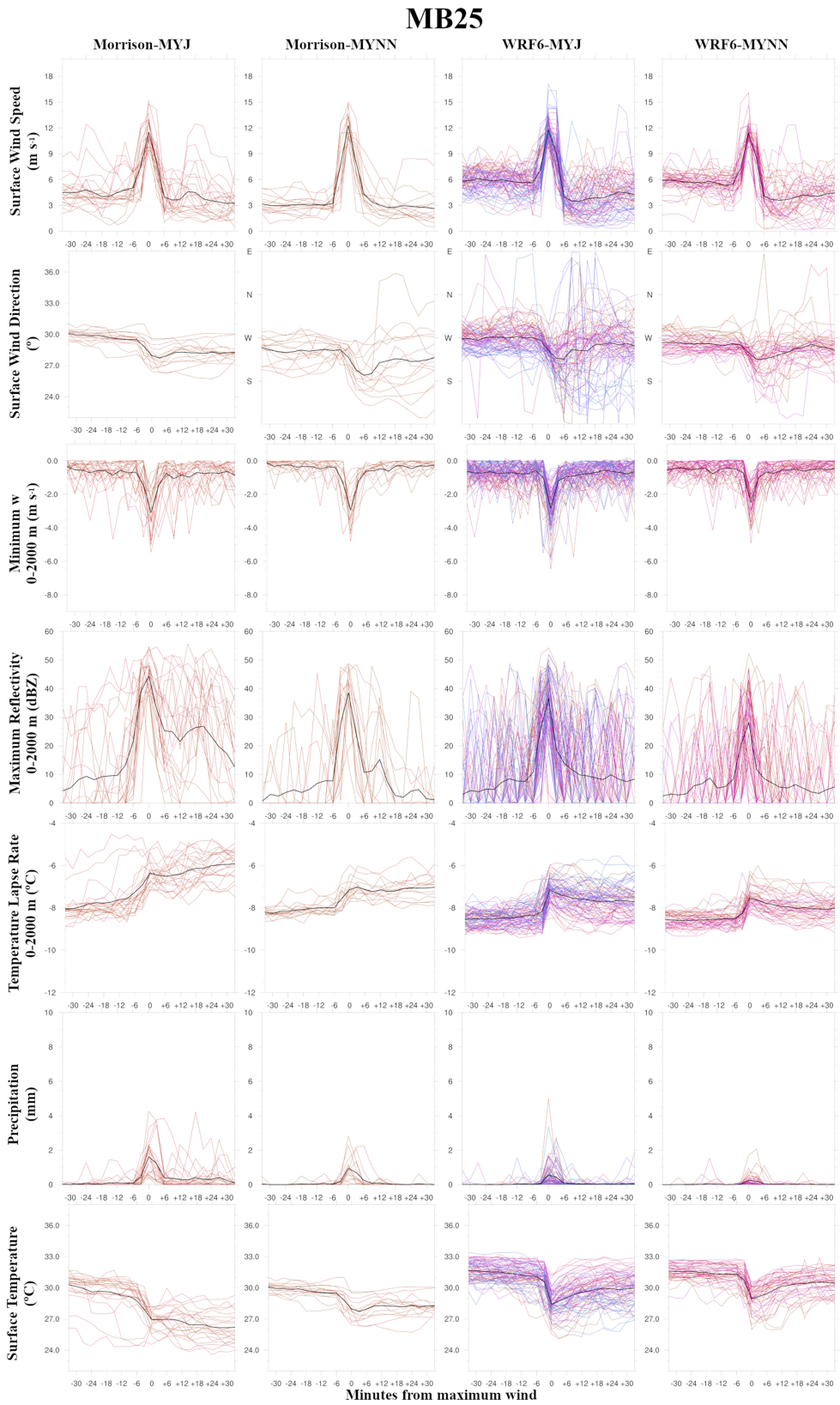

Figure 10. Values for the characteristic variables over the divergence center for each simulated microburst in a ±30 min time window from maximum wind ($t = 0$), for MB25 and every parametrization used. Color lines depict each simulated microburst, black lines depict averages.

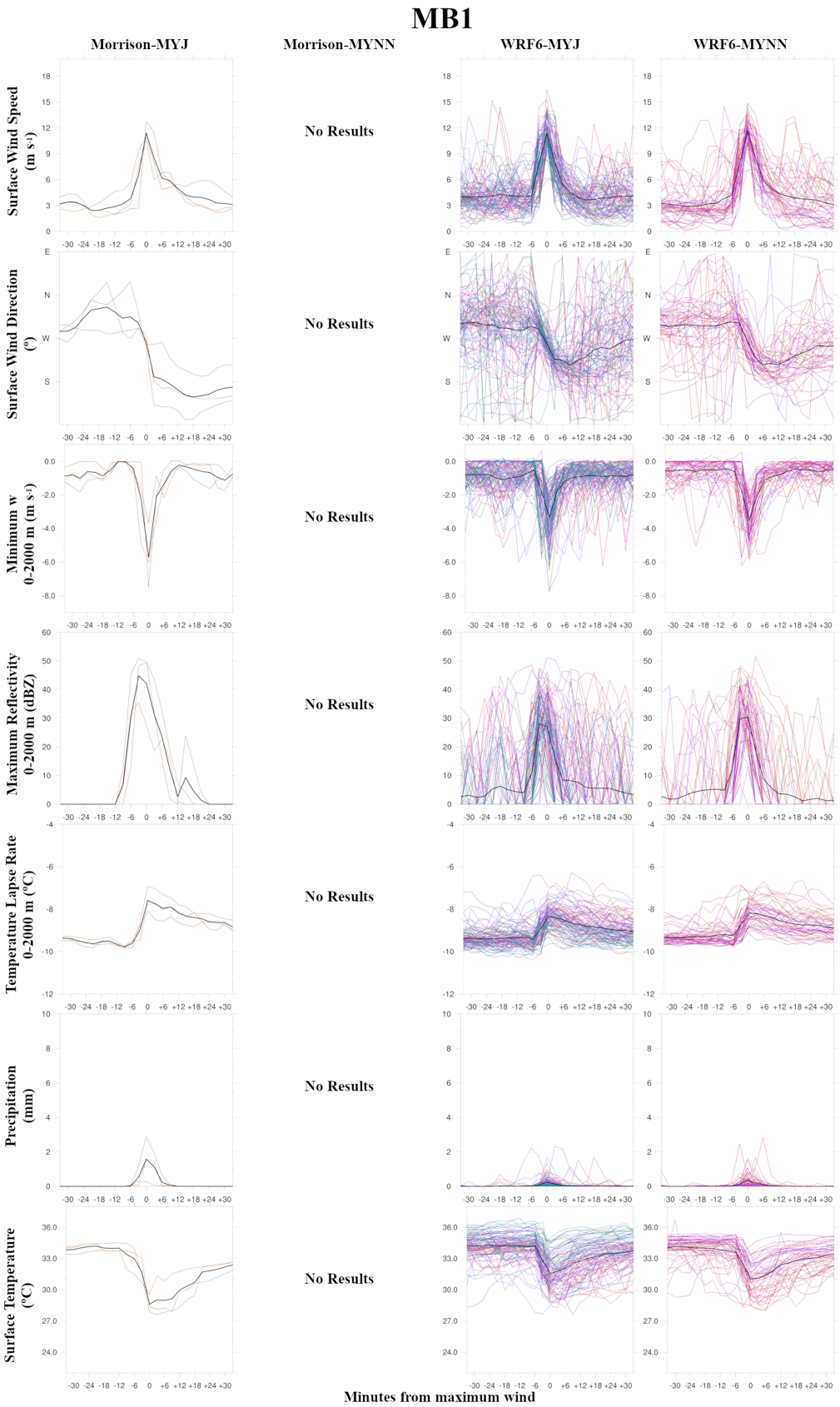

Figure 11. As Figure 10 for MB1.

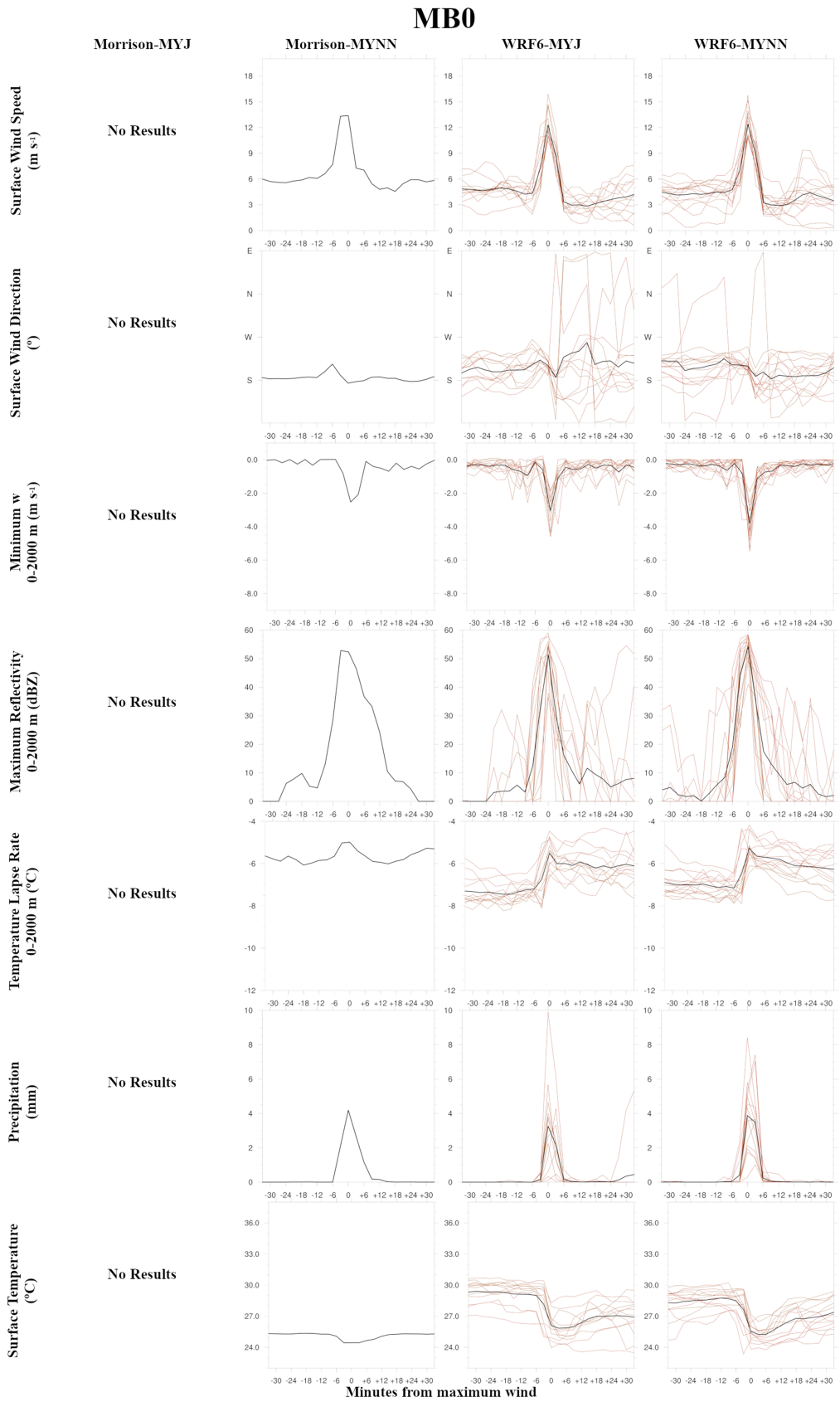

Figure 12. As Figure 10 for MB0.

of the event. Overall, it can be verified in Figures 10, 11, and 12 that the major differences appear between the microphysics parametrizations and not between the PBL parametrizations. In fact, the similarities between the results for WRF6 considering both PBL parametrizations are remarkable. Evaluating the standard deviations for the ±30 min window of each variable (results not shown), it becomes evident that the MYNN PBL parametrization generates a smaller dispersion than the MYJ parametrization, as it yields lower results for the majority of variables and cases. This can be clearly seen in the surface temperature plots for MB25 (Figure 10), where the dispersion values are 0.85 for Morrison-MYNN, 1.00 for WRF6-MYNN, 1.21 for WRF6-MYJ, and 1.47 for Morrison-MYJ. Another example would be the temperature lapse rate for the same date, generating 0.41 for Morrison-MYNN, 0.43 for WRF6-MYNN, 0.55 for WRF6-MYJ, and 0.76 for Morrison-MYJ.

Figure 10 presents the variables for every microburst simulated on MB25. It shows that the average maximum surface wind speed behaves in a pattern similar to the typical process description and complies with the defined wind conditions (Fujita, 1985). The average peak wind speed is approximately 12 m s^{-1}, being this result very consistent for every simulation. The wind speed is more or less stable up to −6 min, returning to approximately the initial speed at +6 min; thus, the event lasts between 6 and 12 min. Both speed and duration are in line with the defined microburst characterization. This would indicate that this variable is properly simulated by the model. Attending to the observations for MB25 (see section 2.1) some discrepancies can be noted. The average maximum wind speed is approximately 3 m s^{-1} lower than the observed speeds, and no simulation shows wind speeds larger than 20 m s^{-1}. To correct the methodical defects stated earlier, the wind gust plots are evaluated for every event and simulation (not shown). The Morrison-MYJ simulation produces two microbursts with gusts over 20 m s^{-1}, while the Morrison-MYNN produces one, the WRF6-MYJ generates nine, and the WRF6-MYNN simulates two. No simulation generates events with wind gusts over 25 m s^{-1} on MB25. Thus, the wind speed variable complies with the characteristics of a microburst but underestimates the maximum intensity. The peak in wind speed is coordinated with a sudden change in wind direction (Figure 10), concurring with the expected microburst process. The rotation is typically less than 90° to a southbound direction from the prevailing western winds. It usually occurs at −3 or 0 min and takes about 15 min to veer back to the original direction. Due to the lack of observations for this variable, it is difficult to evaluate if it is properly simulated.

The minimum negative w component of the wind in the lowest 2,000 m AGL yields mixed results (Figure 10). The sudden onset, timing, and duration of the subsidence are coordinated with the wind speed increase on the surface, reaching the lowest values at 0 min, in line with the genesis of the event (Wilson et al., 1984). Nevertheless, the averages for every simulation are typically over −4 m s^{-1}, and only a few simulated microbursts reach velocities under −6 m s^{-1}. This discrepancy from the characteristic average of −12 m s^{-1} (Hjelmfelt, 1988) makes this variable a weak point for these simulations, which is noteworthy as the w is the main process in the microburst event. Maximum reflectivity for the lowest 2,000 m AGL produces different results for each microphysics parametrization. Every simulation produces a sharp increase in coordination with the maximum wind speed, reaching the maximum reflectivity value at 0 min. This is in accordance with the microburst development and would correspond to the descending reflectivity nucleus (Kingsmill & Wakimoto, 1991; Wakimoto & Bringi, 1988). Averages for the Morrison scheme are above the 35 dBZ threshold. The WRF6 parametrization shows results below the limit, nevertheless, as the variable presents the expected behavior and it is properly coordinated with every other variable, the deficit can be considered negligible.

Temperature lapse rate results (Figure 10) show values below −7.5 °C km^{-1} before the microburst event for every simulation, in agreement with the characterization. A sharp increase of the lapse rate is coincident with the increment of maximum wind speed, and the largest value is typically reached at 0 min, as would expected by the flow of cold air descending from the middle atmosphere (Srivastava, 1985). Afterwards, the variable tends to decrease towards the original value for the WRF6 parametrization but remains the same for the Morrison-MYNN and slightly increases for the Morrison-MYJ. The performance of microphysics parametrizations for precipitation is similar to reflectivity. A maxima is noted at 0 min, as expected per the high-reflectivity microburst development (Srivastava, 1985), Morrison parametrizations clearly exceed the 0.25-mm limit, while the WRF6-MYNN does not reach the minimum. Finally, surface temperature also behaves as expected (Proctor, 1989) although values should be lower. The parcel of air descended from

colder layers of the atmosphere creates a sharp decrease of temperature for almost every simulation, typically around −3 °C, which is above the −4.2 °C average anomaly observed for MB25 (see section 2.1).

The variables for every microburst simulated on MB1 are presented in Figure 11. As evident on Table 1, the Morrison-MYNN simulation produces no microbursts; thus, it generates no results for this case. Evaluating the wind speed, the simulations are very consistent with the results produced for MB25, in behavior, duration of peak winds and wind speed. Wind direction also shows prevailing westerly winds and a change coordinated with the maximum wind speed; although for this case the change is larger than for MB25 (Figure 10), and winds tend to veer back to a more southerly direction than original. The minimum w for the lowest 2,000 m AGL (Figure 11) presents a similar behavior than for MB25, although for MB1 intensities are slightly closer to -4 m s^{-1} for the WRF6 simulations, and the average minimum w is approximately -6 m s^{-1} for the Morrison-MYJ parametrization. Nevertheless, the simulations are far from the characterization, and the variable remains as a weak result for these simulations. Reflectivity once again presents the Morrison-MYN simulations above the 35-dBZ limit, while the WRF6 simulations are below 30 dBZ on average. Temperature lapse rate produces a largely unstable situation for every simulation on MB1, close to being superadiabatic right before the microbursts are simulated. After the event the variable slowly decreases towards its original value. WRF6-MYJ does not comply with the characteristic threshold for precipitation, while the WRF6-MYNN barely reaches it. The surface temperature anomaly behaves similar to reflectivity for MB1. The Morrison-MYJ simulations show a marked drop coordinated to the microburst, close to −6 °C, while the WRF6 simulations present smaller anomalies.

Concerning the variables for MB0, shown on Figure 12, no microburst is simulated by the Morrison-MYJ; thus, it generates no results for the figure. The Morrison-MYNN simulation generates a single microburst with notable differences to the variables described for MB25 (Figure 10) and MB1 (Figure 11). Wind speed and minimum w behave in a similar pattern. Nevertheless, the wind direction shows a southerly flow with a slight change only before the maximum speed, the reflectivity produced is above 50 dBZ, and the precipitation is much larger than for previous cases. At the same time, temperature lapse rate presents a significantly less unstable condition and surface temperature is notably lower; both presenting only slight modifications to the maximum wind speed. All these results show that, despite producing a microburst when none was observed, the simulation is generating a difference in the variables, according to the differences in the thermodynamic situation shown in section 4.1.

The variables for the two WRF6 parametrizations (Figure 12) do not seem to respond in the same way to the changes in the thermodynamic conditions. There are only a few changes from the MB25 and MB1 cases, being the wind direction the most notable. This presents a southerly general flow, seems more chaotic than for the other cases, and does not generate a sharp and coordinated change to the maximum wind speed. Other than that, reflectivities are over 50 dBZ, and surface temperature is slightly lower than the other cases.

4.4. Variables Sensitivity

Table 2 shows the results generated by the detection script (see section 3.3). The assessment of several w intensities (from ground to 2,000 m AGL) once again shows that the model does not reach the characteristic threshold for this variable. As an example, when minimum w is individually tested for MB25, the Morrison-MYJ parametrization produces 0, 43, and 117 warnings for −9, −6, and −3 m s^{-1}, respectively. Imposing a threshold of −6 m s^{-1} yields the best results for this variable, very close to the initial time step count based on divergence for the Morrison-MYJ simulation (Table 1) and once again below the characteristic intensity. However, it has to be considered that the average minimum w for simulated microburst is close to −3 m s^{-1} (Figures 10, 11, and 12), so it can be assumed that most of the times when these w values are detected a microburst is not generated in the surface wind field. This makes this individual variable a poor detection tool.

Evaluating the downburst variables (from ground to 2,000 m AGL), several considerations have to be made. The threshold for w is set at −3 m s^{-1}, as it is the closer value to the average produced by the simulations. It is remarkable the difference between the Morrison and the WRF6 schemes for the temperature lapse rate on MB0. In this case, the Morrison parametrization is performing worse, as the observed thermodynamic diagram shows a low-level instability at 13:00 LT (Atkins & Wakimoto, 1991). It is also notable that, even the temperature lapse rate producing warnings for the majority of time steps, when it is combined with w,

Table 2
Number of Time Steps That Yield Test Warnings as per the Conditions Demanded, for Every Study Case and Parametrization Used

		Downburst (from 0 to 2,000 m AGL)								Outflow					
w (m s^{-1})		≤ −9	≤ −6	≤ −3	—	—	≤ −3	≤ −3	≤ −3						
T Lapse Rate (°C)		—	—	—	≤ −7.5	—	≤ −7.5	—	≤ −7.5						
Reflectivity (dBZ)		—	—	—	—	≥ 35	—	≥ 35	≥ 35						
Wind Speed (m s^{-1})										≥ 10	—	—	≥ 10	≥ 10	≥ 10
T Difference (°C)										—	≤ −4.2	—	≤ −4.2	—	≤ −4.2
Precipitation (mm)										—	—	≥ 0.25	—	≥ 0.25	≥ 0.25
		Positive test results (time steps) for conditions above													
MB25	Morrison-MYJ	0	43	117	185	95	87	87	50	183	43	119	31	80	31
	Morrison-MYNN	0	10	61	190	77	50	60	48	156	7	113	4	49	4
	WRF6-MYJ	0	40	134	202	143	128	127	120	183	116	155	65	122	63
	WRF6-MYNN	0	4	111	223	156	111	103	95	154	50	146	30	73	30
MB1	Morrison-MYJ	1	5	38	140	32	38	25	24	17	17	60	8	15	8
	Morrison-MYNN	0	0	2	140	10	2	1	1	0	0	33	0	0	0
	WRF6-MYJ	7	86	135	140	133	135	124	124	116	109	130	73	81	68
	WRF6-MYNN	5	79	123	140	122	123	113	113	92	83	118	60	77	58
MB0	Morrison-MYJ	0	5	96	0	208	0	84	0	43	0	238	0	16	0
	Morrison-MYNN	0	1	147	0	240	0	125	0	29	0	240	0	19	0
	WRF6-MYJ	0	56	240	161	240	36	236	13	161	119	240	5	156	5
	WRF6-MYNN	0	30	240	124	240	15	240	0	122	85	240	4	121	4

almost no event is detected. This shows that w is governing the sensitivity of the variables. When reflectivity is added to the combination, there are no drastic changes, but the results are improved. The combination of the three variables yields the best detection results for downburst. Assessing the parametrizations, the Morrison-MYNN simulation is the best performer in detecting the downburst, as the results are closer to the number of observed microbursts.

When the outflow variables are analyzed the surface temperature anomaly shows the better sensitivity to detect microbursts. For this variable, Morrison-MYJ shows a good correlation with the thermodynamic situation (see section 4.1) and the initial microburst count (Table 1). The surface wind speed and precipitation tend to reach the characteristic thresholds in many time steps. The combination of variables presents the best results when using the wind speed and temperature anomaly. The precipitation adds no useful information, as almost no difference can be seen when the three variables are combined. Regarding the parametrizations, the Morrison-MYJ performs best in detecting the outflow, as it yields a number of events closer to observations.

5. Conclusions

In this study, several episodes of high-reflectivity microbursts are simulated using the WRF model at spatial resolutions of 400 m and temporal resolutions of 3 min. Different microphysics and PBL parametrizations are tested to find the best model configuration for these events. Every parametrization used seems to capture the thermodynamic diagrams, the diurnal variation, and the characteristic variables of the microburst. The timing and coordination between variables are according to observations and characteristic process. Also the average values are in agreement with the characteristic thresholds, although there is a tendency to underestimate intensities, most notable for w. The dynamics of the microburst are properly reproduced too, with a good simulation of dimensions, time span, and dynamic development of events.

The Morrison microphysics scheme slightly outperforms the WRF6 parametrization in the modeling of the variables, although differences are not remarkable. As variables cannot be used as a definitive discriminator, the total number of microburst simulated remains the main difference between parametrizations. When this is considered, the Morrison parametrization clearly outperforms the WRF6. The sensitivity of the variables and the number of microbursts simulated by the WRF6 microphysics scheme do not seem to present a correlation with the different thermodynamic situation of each day, although these are properly reproduced. The Morrison-MYJ yields better results in the total count and performs better in capturing the outflow

when the variables' thresholds are considered. The Morrison-MYNN produces better results in the simulation of the variables related to the downburst and tends to simulate more uniform events as it has lower dispersion values.

One important issue requiring further study is the simulation of w. The analysis performed in this paper leads to the conclusion that the WRF model largely underestimates the intensity of this variable. Nevertheless, when the scientific literature is reviewed, it can be noted that the fist value proposed is just a mere $-3.6\ \mathrm{m\ s^{-1}}$. Although the characterization of this variable for the microburst is much larger, no study states a specific minimum value. At the light of the results of this paper, with an average w value very close to the aforementioned figure, it may be considered if high-reflectivity microbursts can develop with weaker w intensities than expected by the present knowledge.

Overall, it can be concluded that the WRF properly simulates the variables and dynamics of a high-reflectivity microburst. Although the results may appear to be suboptimal, it has to be considered that the WRF is a mesoscale model, not optimized to simulate microscale events. It has also to be noted that the microburst is a complex event, governed by several microphysics processes and atmospheric variables very sensitive to small changes, and in turn to natural variability, which renders it a meteorological phenomenon very hard to prognosticate in exact time and position even using real time data. When accounting for the internal variability, it cannot be expected for the model to simulate exactly the same number of microbursts, in the exact area and times. Thus, the simulations yielded by the Morrison-MYJ and the Morrison-MYNN parametrizations are close enough to observations to consider them as good performers.

Further research is required to fine-tune the WRF model for microburst detection, which will also depend on the geographical area of study. No specific variable shows the sensitivity required to be used as a prognostic tool. Nevertheless, the authors consider that using the available data and numerical predicting models, forecasting algorithms may already be viable. The application of existing warning indices and forecasting algorithms on numerical prediction models may be studied. From the results of this paper, the sharp variation over short periods of variables as surface wind divergence, temperature lapse rate, w, or Θ_e should be considered as possible precursors. Another possibility is to develop a forecasting algorithm based on different detection phases, which may use several simulations according to the performance of each parametrization for each microburst phase.

Acknowledgments
The authors declare no conflict of interest. The founding sponsors have no participation in the execution of the experiment, the decision to publish the results, nor in the writing of the manuscript. This work is supported by the Interdisciplinary Mathematics Institute of the Complutense University of Madrid and the following research projects: METEORISK (RTC-2014-1872-5), PCIN-2014-013-C07-04, PCIN-2016-080 (UE ERANET Plus NEWA Project), ESP2013-47816-C4-4-P, CGL2010-15930, CGL2016-81828-REDT, FEI-EU-17-16, and SAFEFLIGHT (CGL2016-78702-C2-1-R and CGL2016-78702-C2-2-R). This research is founded by the Spanish Ministry of Economy and Enterprise under the framework of the SAFEFLIGHT research project (CGL2016-78702-C2-1-R and CGL2016-78702-C2-2-R). The data used to support the conclusions of this paper are model outputs mainly. Model configuration scripts, data processing scripts, and processed data are available for further examination (https://doi.10.17632/xfxkpsg4mc.1). As this paper is part of an ongoing research at the time of publication, the dataset may be under a provisional embargo.

References

Atkins, N. T., & Wakimoto, R. M. (1991). Wet microburst activity over the southeastern United States: Implications for forecasting. *Weather and Forecasting*, *6*(4), 470–482. https://doi.org/10.1175/1520-0434(1991)006<0470:WMAOTS>2.0.CO;2

Atlas, D., Ulbrich, C. W., & Williams, C. R. (2004). Physical origin of a wet microburst: Observations and theory. *Journal of the Atmospheric Sciences*, *61*(10), 1186–1195. https://doi.org/10.1175/1520-0469(2004)061<1186:POOAWM>2.0.CO;2

Bolgiani, P., Fernández-González, S., Valero, F., Merino, A., García-Ortega, E., Sánchez, J. L., & Martín, M. L. (2018). Numerical simulation of a heavy precipitation event in the vicinity of Madrid-Barajas International Airport: Sensitivity to initial conditions, domain resolution, and microphysics parameterizations. *Atmosphere*, *9*(9), 24. https://doi.org/10.3390/atmos9090329

Burlando, M., Romanić, D., Solari, G., Hangan, H., & Zhang, S. (2017). Field data analysis and weather scenario of a downburst event in Livorno, Italy, on 1 October 2012. *Monthly Weather Review*, *145*(9), 3507–3527. https://doi.org/10.1175/MWR-D-17-0018.1

Byers, H. R., & Braham, R. R. (1949). *The thunderstorm*. Washington, DC: U.S. Government Printing Office.

Caplan, S. J., Bedard, A. J., & Decker, M. T. (1990). The 700–500 mb lapse rate as an index of microburst probability: An application for thermodynamic profilers. *Journal of Applied Meteorology*, *29*(8), 680–687. https://doi.org/10.1175/1520-0450(1990)029<0680:TMLRAA>2.0.CO;2

Carroll, D., Hollings, E. F., Garrett, G., Carpenter, E., Weather, N., & Jackson, S. (2011). *WRF optimization for forecasting wet microburst potential*. Abstract presented at *American Geophysical Union, Fall Meeting 2011*, A51A-0148.

Chou, M., & Suarez, M. (1999). A solar radiation parameterization (CLIRAD-SW) for atmospheric studies. In *NASA Tech. Memo* (Vol. 10460). Greenbelt, MD.

Chou, M., Suarez, M., Liang, X., & Yan, M. (2001). A thermal infrared radiation parameterization for atmospheric studies. In *NASA Technical Report* (Vol. *19*). Greenbelt, MD.

Creighton, G., Kuchera, E., Adams-Selin, R., McCormick, J., Rentschler, S., & Wickard, B. (2014). AFWA Diagnostics in WRF.

van Dijke, D., Hinssen, Y., & Bijlsma, F. (2011). A 500 m WRF hindcast of a microburst event in The Netherlands. Abstract presented at *European Meteorological Society Annual Meeting*, EMS2011-546-1, 8, 1–4.

Dodge, J., Arnold, J., Wilson, G., Evans, J. P., & Fujita, T. T. (1986). The cooperative Huntsville Meteorological Experiment (COHMEX). *Bulletin of the American Meteorological Society*, *67*(4), 417–419.

Ferrero, E., Mortarini, L., Manfrin, M., Solari, M., & Forza, R. (2014). Physical simulation of atmospheric microbursts. *Journal of Geophysical Research: Atmospheres*, *119*, 6292–6305. https://doi.org/10.1002/2013JD021243

Fujita, T. T. (1976). Spearhead echo and downburst near the approach end of a John F. Kennedy Airport runway. Chicago, IL.

Fujita, T. T. (1980). Downbursts and microbursts, an aviation hazard. *19th Conference on Radar Meteorology*, 8. Miami Beach, FL: American Meteorological Society.
Fujita, T. T. (1981a). Microbursts as an aviation wind shear hazard. *19th Aerospace Sciences Meeting*, 9. St. Louis, MO: American Institute of Aeronautics and Astronautics.
Fujita, T. T. (1981b). Tornadoes and downbursts in the context of generalized planetary scales. *Journal of the Atmospheric Sciences*, *38*(8), 1511–1534. https://doi.org/10.1175/1520-0469(1981)038<1511:TADITC>2.0.CO;2
Fujita, T. T. (1985). The downburst: Microburst and macroburst. In *SMRP Research Papers* (Vol. *210*). Chicago, IL.
Fujita, T. T., & Byers, H. R. (1977). Spearhead echo and downburst in the crash of an airliner. *Monthly Weather Review*, *105*(2), 129–146. https://doi.org/10.1175/1520-0493(1977)105<0129:seadit>2.0.co;2
Fujita, T. T., & Wakimoto, R. M. (1981). Five scales of airflow associated with a series of downbursts on July 16, 1980. *Monthly Weather Review*, *109*(7), 1438–1456. https://doi.org/10.1175/1520-0493(1981)109<1438:FSOAAW>2.0.CO;2
Fujita, T. T., & Wakimoto, R. M. (1983). JAWS microbursts revealed by triple-Doppler radar, aircraft, and PAM data. *13th Conference on Severe Local Storms*, 4.
Grell, G., & Freitas, S. R. (2014). A scale and aerosol aware stochastic convective parameterization for weather and air quality modeling. *Atmospheric Chemistry and Physics*, *14*(10), 5233–5250. https://doi.org/10.5194/acp-14-5233-2014
Hjelmfelt, M. R. (1988). Structure and life cycle of microburst outflows observed in Colorado. *Journal of Applied Meteorology*, *27*(8), 900–927.
Hong, S.-Y., & Lim, J.-O. J. (2006). The WRF single–moment 6–class microphysics scheme (WSM6). *Journal of the Korean Meterological Society*, *42*, 129–151.
James, R. P., & Markowski, P. M. (2010). A numerical investigation of the effects of dry air aloft on deep convection. *Monthly Weather Review*. https://doi.org/10.1175/2009MWR3018.1
Janjic, Z. I. (1994). The step-mountain eta coordinate model: Further developments of the convection, viscous sublayer, and turbulence closure schemes. *Monthly Weather Review*, *122*, 927–945. https://doi.org/10.1175/1520-0493(1994)122<0927:TSMECM>2.0.CO;2
Johns, R. H., & Doswell, C. A. (1992). Severe local storms forecasting. *Weather and Forecasting*, *7*, 588–612.
Kelly, D. L., Schaefer, J. T., & Doswell, C. A. (1985). Climatology of nontornadic severe thunderstorm events in the United States. *Monthly Weather Review*, *113*(11), 1997–2014. https://doi.org/10.1175/1520-0493(1985)113<1997:CONSTE>2.0.CO;2
Kessinger, C. J., Parsons, D. B., & Wilson, J. W. (1988). Observations of a storm containing misocyclones, downbursts, and horizontal vortex circulations. *Monthly Weather Review*, *116*(10), 1959–1982. https://doi.org/10.1175/1520-0493(1988)116<1959:OOASCM>2.0.CO;2
Kingsmill, D. E., & Wakimoto, R. M. (1991). Kinematic, dynamic, and thermodynamic analysis of a weakly sheared severe thunderstorm over northern Alabama. *Monthly Weather Review*, *119*(2), 262–297. https://doi.org/10.1175/1520-0493(1991)119<0262:KDATAO>2.0.CO;2
Knupp, K. (1988). Downdrafts within high plains cumulonimbi. Part II: Dynamics and thermodynamics. *Journal of the Atmospheric Sciences*, *45*(24), 3965–3982. https://doi.org/10.1175/1520-0469(1988)045<3965:DWHPCP>2.0.CO;2
Lin, W. E., Orf, L. G., Savory, E., & Novacco, C. (2007). Proposed large-scale modelling of the transient features of a downburst outflow. *Wind and Structures, An International Journal*, *10*(4), 315–346. https://doi.org/10.12989/was.2007.10.4.315
McCann, D. W. (1994). WINDEX—A new index for forecasting microburst potential. *Weather & Forecasting*, *9*(4), 532–541. https://doi.org/10.1175/1520-0434(1994)009<0532:WNIFFM>2.0.CO;2
McCarthy, J., Wilson, J. W., & Fujita, T. T. (1982). The joint airport weather studies project. *Bulletin of the American Meteorological Society*, *63*(1), 15–22.
Morrison, H., Thompson, G., & Tatarskii, V. (2009). Impact of cloud microphysics on the development of trailing stratiform precipitation in a simulated squall line: Comparison of one- and two-moment schemes. *Monthly Weather Review*, *137*(3), 991–1007. https://doi.org/10.1175/2008MWR2556.1
Nakanishi, M., & Niino, H. (2006). An improved Mellor-Yamada Level-3 model: Its numerical stability and application to a regional prediction of advection fog. *Boundary-Layer Meteorology*, *119*(2), 397–407. https://doi.org/10.1007/s10546-005-9030-8
NCAR (2019). *NCAR command language*. https://doi.org/10.5065/D6WD3XH5
NWS (2019). National Weather Service Monthly Weather Summary for Huntsville Airport. Retrieved February 24, 2019, from https://w2.weather.gov/climate/index.php?wfo=hun
Ohno, H., Suzuki, O., & Kusunoki, K. (1996). Climatology of downburst occurrence in Japan. *18th Conference on Severe Local Storms*, 87–90.
Oreskovic, C., Orf, L. G., & Savory, E. (2018). A parametric study of downbursts using a full-scale cooling source model. *Journal of Wind Engineering and Industrial Aerodynamics*. https://doi.org/10.1016/j.jweia.2018.07.020
Orf, L., Kantor, E., & Savory, E. (2012). Simulation of a downburst-producing thunderstorm using a very high-resolution three-dimensional cloud model. *Journal of Wind Engineering and Industrial Aerodynamics.*. https://doi.org/10.1016/j.jweia.2012.02.020
Potts, R. J. (1991). Microburst observations in tropical Australia. *25th Internation Conference on Radar Meteorology*, J67–J72.
Proctor, F. H. (1988). Numerical simulations of an isolated microburst. Part I: Dynamics and structure. *Journal of the Atmospheric Sciences*, *45*(21), 3137–3160. https://doi.org/10.1175/1520-0469(1988)045<3137:NSOAIM>2.0.CO;2
Proctor, F. H. (1989). Numerical simulations of an isolated microburst. Part II: Sensitivity experiments. *Journal of the Atmospheric Sciences*, *46*(14), 2143–2165. https://doi.org/10.1175/1520-0469(1989)046<2143:NSOAIM>2.0.CO;2
Pryor, K. L. (2015). Progress and developments of downburst prediction applications of GOES. *Weather and Forecasting*, *30*(5), 1182–1200. https://doi.org/10.1175/WAF-D-14-00106.1
Pryor, K. L., & Ellrod, G. P. (2004). WMSI—A new index for forecasting wet microburst severity. *National Weather Association Electronic Journal of Operational Meteorology*, *25*.
Roberts, R. D., & Wilson, J. W. (1989). A proposed microburst nowcasting procedure using single-Doppler radar. *Journal of Applied Meteorology*, *28*, 285–303. https://doi.org/10.1175/1520-0450(1989)028<0285:APMNPU>2.0.CO;2
Rydell, N. N., & Ladd, J. W. (1991). Toward a climatology of south Texas downbursts. *4th International Conference on Aviation Weather Systems*, 169–173. Paris, France.
Saha, S., Nadiga, S., Thiaw, C., Wang, J., Wang, W., Zhang, Q., ... Xie, P. (2010). NCEP Climate Forecast System Reanalysis (CFSR) 6-hourly Products, *January 1979 to December 2010*. https://doi.org/10.5065/D69K487J
Skamarock, W. C., & Klemp, J. B. (2008). A time-split nonhydrostatic atmospheric model for weather research and forecasting applications. *Journal of Computational Physics*, *227*(7), 3465–3485. https://doi.org/10.1016/j.jcp.2007.01.037
Skamarock, W. C., Klemp, J. B., Dudhia, J., Gill, D. O., Barker, D. M., Duda, M. G., ... Powers, J. G. (2008). A description of the advanced research WRF Version 3. *NCAR Technical Note NCAR/TN-475 + STR*, p. 113. https://doi.org/10.5065/D68S4MVH

Srivastava, R. C. (1985). A simple model of evaporatively driven downdraft: Application to microburst downdraft. *Journal of the Atmospheric Sciences*, *42*(10), 1004–1023. https://doi.org/10.1175/1520-0469(1985)042<1004:ASMOED>2.0.CO;2

Srivastava, R. C. (1987). A model of intense downdrafts driven by the melting and evaporation of precipitation. *Journal of the Atmospheric Sciences*, *44*(13), 1752–1773.

Tewari, M., Chen, F., Wang, W., Dudhia, J., LeMone, M. A., Mitchell, K., ... Cuenca, R. H. (2004). Implementation and verification of the unified NOAH land surface model in the WRF model. *20th Conference on Weather Analysis and Forecasting/16th Conference on Numerical Weather Prediction*, 10–15. Seattle, WA: American Meteorological Society.

Vermeire, B. C., Orf, L. G., & Savory, E. (2011a). A parametric study of downburst line near-surface outflows. *Journal of Wind Engineering and Industrial Aerodynamics*, *99*(4), 226–238.

Vermeire, B. C., Orf, L. G., & Savory, E. (2011b). Improved modelling of downburst outflows for wind engineering applications using a cooling source approach. *Journal of Wind Engineering and Industrial Aerodynamics*. https://doi.org/10.1016/j.jweia.2011.03.003

Wakimoto, R. M. (1985). Forecasting dry microburst activity over the high plains. *Monthly Weather Review*, *113*(7), 1131–1143. https://doi.org/10.1175/1520-0493(1985)113<1131:FDMAOT>2.0.CO;2

Wakimoto, R. M. (2001). Convectively driven high wind events. In C. A. Doswell (Ed.), *Severe convective storms* (Vol. 50, pp. 255–298). Boston, MA: American Meteorological Society. https://doi.org/10.1007/978-1-935704-06-5_7

Wakimoto, R. M., & Bringi, V. N. (1988). Dual-polarization observations of microbursts associated with intense convection: The 20 July storm during the MIST project. *Monthly Weather Review*, *116*(8), 1521–1539. https://doi.org/10.1175/1520-0493(1988)116<1521:DPOOMA>2.0.CO;2

Wakimoto, R. M., Kessinger, C. J., & Kingsmill, D. E. (1994). Kinematic, thermodynamic, and visual structure of low-reflectivity microbursts. *Monthly Weather Review*, *122*(1), 72–92. https://doi.org/10.1175/1520-0493(1994)122<0072:KTAVSO>2.0.CO;2

Wilson, J. W., Roberts, R. D., Kessinger, C. J., & McCarthy, J. (1984). Microburst wind structure and evaluation of Doppler radar for airport wind shear detection. *Journal of Climate & Applied Meteorology*, *23*(6), 898–915. https://doi.org/10.1175/1520-0450(1984)023<0898:MWSAEO>2.0.CO;2

Wolfson, M. M. (1990). Understanding and predicting microbursts. Massachusetts Institute of Technology.

Wolfson, M. M., Delanoy, R. L., Forman, B. E., Hallowell, R. G., Pawlak, M. L., & Smith, P. D. (1994). Automated microburst wind-shear prediction. *The Lincoln Laboratory Journal*, *7*(2), 399–426.

Wolfson, M. M., DiStefano, J. T., & Fujita, T. T. (1985). Low-altitude wind shear in the Memphis, TN area based on mesonet and LLWAS data. *14th Conference on Severe Local Storms*, 322–327. Indianapolis, IN: American Meteorological Society.